UNIVERSIDADE Đ COIMBRA

Diogo Miguel Pereira da Fonseca

FORCE/PROXIMITY HYBRID SENSORS
AND
PHASE CHANGE ACTUATORS

Setembro de 2021

FORCE/PROXIMITY HYBRID SENSORS AND PHASE CHANGE ACTUATORS

Submitted in partial fulfilment of the requirements for the Degree of Master in Mechanical Engineering in the speciality of Production and Project

Sensores híbridos de força/proximidade e atuadores de mudança de fase

Author
Diogo Miguel Pereira da Fonseca

Advisor
Pedro Mariano Simões Neto

Jury

President	**Professor Doutor José Luís Ferreira Afonso** **Professor Auxiliar da Universidade de Coimbra**
Vowels	**Professor Doutor Mohammad Safeea** **Professor Convidado da Universidade de Coimbra** **Professor Doutor Pedro Mariano Simões Neto.** **Professor Auxiliar da Universidade de Coimbra**
Advisors	**Professor Doutor Pedro Mariano Simões Neto.** **Professor Auxiliar da Universidade de Coimbra**

Coimbra, September, 2021

Force/Proximity Hybrid Sensors
and
Phase Change Actuators

A thesis submitted to the University of Coimbra
for the degree of Master of Science in the
Faculty of Science and Technology
2021

Diogo Miguel Pereira da Fonseca

Department of Mechanical Engineering

Abstract

Insightful perception of the surrounding environment, as well as compliant mechanisms are two important goals to enable safe and intuitive Human-Robot Interaction (HRI). This work is divided into two parts. In Part 1, a mechanically flexible, piezoresistive and self-capacitive hybrid force and proximity sensor is presented. Made of low cost and highly available components, the proposed sensor can be economically made and deployed in large numbers, improving the sensory awareness of any robotic system. A Data Acquisition System (DAQ) was also presented, allowing users to conveniently interface the sensor through a regular Universal Serial Bus (USB) connection. Results show a fast and moderately precise response to forces ranging between 0.5 N and 15 N. Human presence detection was achieved at distances up to 100 mm, but with fairly low spatial resolution (~50 mm).

In Part 2 of this work, a compliant Phase Change Artificial Muscle (PCAM) is presented. Based on traditional pneumatic McKibben Pneumatic Artificial Muscles (PAMs), the proposed actuator explores the volumetric expansion of water undergoing liquid-gas phase transition, powered by a low voltage DC power source. Actuation forces of 27.5 N were routinely achieved with actuators weighing just 23 g. High pressure control precision was achieved, with the system following set pressure commands within +- 1 kPa. Several important phenomena were explored and discussed including limits to pressurization rates, fluid safety and control limitations, laying the foundation for future development and deployment.

Keywords: Compliance, Soft Robotics, Force Sensing Resistor, Piezoresistive Sensor, Proximity Sensor, Force Sensor, Actuator, Soft Actuator, Phase Change Actuator, Pneumatic Artificial Muscle.

Resumo

A perceção eficaz do ambiente envolvente, assim como a criação de mecanismos flexíveis são dois objetivos importantes para alcançar uma interação homem-robô (*Human-Robot Interaction* – HRI) segura e intuitiva. Este trabalho encontra-se dividido em duas partes. Na primeira parte apresentamos um sensor híbrido de força e proximidade, mecanicamente flexível, baseado nos fenómenos de piezoresistividade e capacidade elétrica. Constituído por materiais e componentes de baixo custo, amplamente disponíveis no mercado, o sensor proposto pode ser fabricado e implementado de forma económica em grande escala, melhorando a perceção sensorial de qualquer instalação robótica. Um sistema de aquisição de dados (*Data Acquisition System* – DAQ) foi também apresentado, permitindo uma interface conveniente com sensor, por meio de uma conexão série USB (*Universal Serial Bus*). Resultados demonstraram uma resposta rápida e moderadamente precisa a forças entre 0,5 N e 15 N. A deteção de presença humana foi alcançada a distâncias de até 100 mm, embora com uma resolução espacial relativamente reduzida (~ 50 mm).

Na segunda parte deste trabalho apresentamos um atuador flexível baseado no processo de mudança de fase (*Phase Change Artificial Muscle* – PCAM). Com base em músculos artificiais pneumáticos tradicionais McKibben (*Pneumatic Artificial Muscles* – PAMs), o atuador proposto explora a expansão volumétrica da água em transição de fase líquido-vapor alimentada por uma fonte de alimentação DC (*Direct Current*) de baixa tensão. Forças de atuação de 27,5 N foram repetidamente alcançadas com atuadores cuja massa é de apenas 23 g. Alta precisão no controlo de pressão foi alcançada, com o sistema a apresentar-se capaz de seguir comandos de pressão com erros de + - 1 kPa. Vários fenómenos importantes foram explorados e discutidos, incluindo limites para taxas de pressurização, segurança de fluidos e limitações de controlo, estabelecendo uma base sólida para futuro desenvolvimento e aplicação.

Declaration

No portion of this thesis has been submitted in support of an application for another degree or qualification of this or any other university or other institute of learning.

Acknowledgments

Contents

List of Figures

Accompanying Materials

Support Material 01 – Calculation Procedure of Work/Heat Quotient During Isobaric Liquid-Gas Phase Transition.

Support Material 02 – Calculation of Inflatable Bladder Minimum Tube Length

Support Material 03 – Cover Factor of a Biaxial Braided Sleeve

Support Material 04 – Actuator Static Model

"I am hitting my head against the walls, but the walls are giving way"
– Gustav Mahler

Part I

Flexible Force and Proximity Hybrid Sensors

Chapter 1

Motivation and Basic Principles

1.1 Introduction

ADVANCED robots increasingly require more sensors to perceive their surroundings. Robot sensors are key to successful and intuitive human-robot interaction (HRI) and robot autonomy. However, many times, the existing conventional sensors are limited and do not fit the specific robot and application requirements [3]. Conventional sensors have limitations that are related to their inability to measure variables of interest, insufficient accuracy and/or robustness in working conditions. For example, vision sensors are constrained by light and suffer from occlusions. Other sensors may be limited by the response time or repeatability. Frequently, researchers and engineers are looking for hybrid single sensor devices that are able to measure the parameters they are looking for, and which are easy to install on a robot's structure or in the robot's surroundings. The problem is that these sensors are not normally available. Existing sensors frequently require costly alterations to reach hybrid, integrated solutions and they are not mechanically flexible, which makes them difficult to integrate on robot structures with complex geometries.

The robotics and artificial intelligence markets are rapidly growing and sensors have a main role in their success [65]. Such a scenario is important in a context where robots increasingly operate in more unstructured environments and interact with humans in a more natural way. Tactile/force and proximity sensing are features that are desired for robot safety and interaction [30]. The ISO/TS 15066 standard for collaborative robot safety depends significantly on the robot's ability to detect the presence of humans or objects within the robot's surroundings, especially

for speed and separation monitoring [46]. In such a context, hybrid force and proximity sensors, which are easily installable on pre-existing robot systems, are extremely desirable. Nevertheless, an integrated development, manufacturing at an affordable cost and reliability are challenging objectives to achieve.

This thesis proposes a novel mechanically flexible piezoresistive and self-capacitive hybrid force and proximity sensor that is easy to apply on any robotic system in the same way that humans apply masking tape to a surface. The manufacturing process is described step by step, including the electronics, mechanical design and data acquisition. Trials featuring the characterization of the sensor were conducted, focusing on both the force-electrical resistance relationship and self-capacitive proximity response. The proposed sensor was evaluated and successfully applied in two distinct situations: hand guiding a robot (measuring the touch force and proximity to the hand), and collision avoidance (measuring the proximity to the hand).

Experimental tests resulted in the following contributions:

1. A novel mechanically flexible piezoresistive/self-capacitive hybrid force and proximity sensor.

2. The sensor's structure is mechanically flexible making it as easy to use and apply as masking tape.

3. The sensor is relatively easy to manufacture at a low cost (the process is detailed here step by step).

4. The sensor provides reasonable accuracy and repeatability concerning force and proximity measurements. The presence of a human hand is detected at up to 100 mm away, the minimum force is 0.5 N and the single point repeatability is about 11%.

5. The sensor's versatility, flexibility and accuracy demonstrated applicability in other fields besides robotics.

1.2 Related Work

The simultaneous sensing of capacitive and inductive proximity by a single sensor device has been studied recently [36]. Dual-mode sensors (capacitive and inductive) have demonstrated the ability to measure tactile pressure of up to 330 kPa and sense proximity with a good spatial resolution (3 mm) at distances of up to 150 mm [16]. Sensitive artificial skins

capable of detecting contact forces have proved adaptable for use with Force-sensing Resistor (FSR) sensors [59]. Recent research has shown the potential of using commercially available FSRs for proximity sensing, taking advantage of the electrodes already present in the FSR to perform capacitive proximity sensing [9]. A robot skin made of soft porous materials (elastomer and wrapped around a textile) has been shown to be able to measure distributed contact force [40]. A novel piezoresistive pressure sensor to measure low pressures is proposed in [57]. The sensor is fabricated using an n-type single-crystal silicon wafer, with photolithography to fabricate the sensing elements and the piezoresistors are formed by boron implantation. A piezoresistive sensor array made of conductive polymer composite detects not only the pressure applied on the electrode but also the pressure applied on the areas among the sub-elements, eliminating the blind areas [61]. A tactile sensor based on giant magneto-impedance material embedded with an air gap has performed well when implemented in smart prosthetics [64]. Capacitive sensing has been successfully used as a base technology for diverse sensors measuring angular position [60] and proximity [36]. Proximity values can be obtained by measuring the electrostatic capacity in conductive flexible fabric [31]. Recently, conductive elastomers were studied to address the challenges of sensing deformable soft structures [22]. With the aim of low cost, large-scale production, they are directly fabricated onto fabric substrates [63]. Smart conductive textiles are increasingly used in wearable electronics. Recent studies adjust their modeling to compensate for intrinsic nonlinearities, namely, hysteresis and relaxation [39]. Programmable sensor networks have been integrated modularly in the form of a tape (flexible electronics substrate) [12]. Proximity, contact and force can be measured by arrays of proximity sensors (flexible printed circuit boards) embedded in silicone [20]. However, although they provide reliable data, their flexibility is limited and their fabrication is relatively costly and complex.

1.3   Background and Design Principals

When a conductive material is deformed, its electrical resistance changes. Assuming the material's volume resistivity remains constant, the electrical resistance could be estimated from its cross-sectional area and length. This is the underlying principle behind various sensors, such as resistive strain gauges [15]. However, semi-conductive polymer composites, such as Caplinq's Linqstat or 3M's Velostat, behave differently. Their electrical resistivity changes (drastically) under strain. Conductive filler particles are randomly dispersed in a nonconductive polymeric matrix inside those
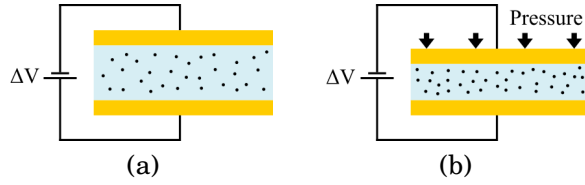
Figure 1.1: Compression of a semi-conductive polymer. a) Uncompressed.
b) Compressed.
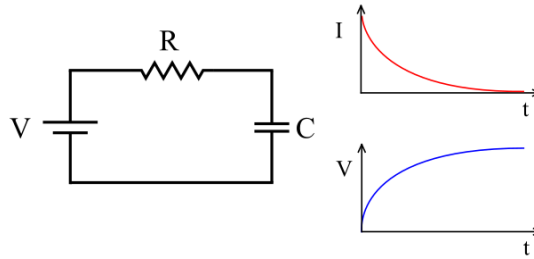
Figure 1.2: Resistor-Capacitor (R-C) circuit.

composites, Fig. 1.1.

When compressed, those particles move randomly closer together through
what is known as micro-Brownian motion [29]. On the one hand, this
leads to a higher number of particles contacting each other, creating more
paths for electricity to flow and thus lowering resistivity. On the other
hand, the particles that are not in direct contact become, on average,
separated by shorter distances. This elevates the number of electrons
tunneling through the non-conductive matrix between filler particles, re-
ducing the polymer's resistivity even further [49]. In this scenario, the
sensor's electrical resistance range will not be of just a few percent (as in
resistive strain gauges), but indeed may range across multiple orders of
magnitude.

Most proximity sensors are based on optical, ultrasonic or capacitive tech-
nology. Since we were looking for a thin and flexible sensor, ultrasonic
sensing was considered impractical. LEDs paired with photoresistors
could be used for optical sensing but would also compromise our design
goals (thin and flexible). Off-the-shelf FSRs have recently been used for
capacitive proximity sensing [9]. The self-capacitance phenomenon will
be explored in our proposed sensor.

Fig. 1.2 shows a parallel plate capacitor circuit where, after an initial
transient period, a steady-state is reached. The potential across the ca-
pacitor's terminals opposes the power supply voltage and, at that point,
there is no longer electric current flowing through the system. A similar

15
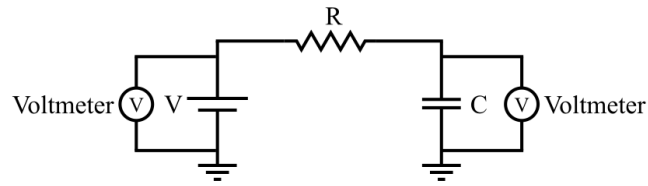
Figure 1.3: R-C circuit with common ground.
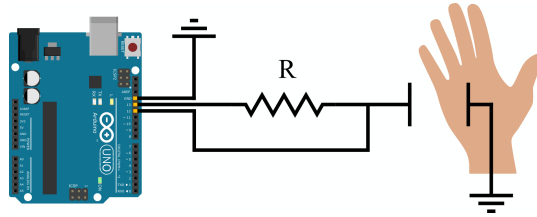
Figure 1.4: Proximity sensing.

circuit may be considered, Fig. 1.3, where after a certain time, both the power supply and the capacitor will tend to reach symmetric potential differentials.

The resistor wired in series limits the current flowing through the circuit during the initial transient period, prolonging the amount of time necessary to reach a stationary state. Considering that a parallel plate capacitor is essentially composed of two conductive plates separated by an insulating medium, either a dielectric material or vacuum, then if we allow the insulating medium to be air and the grounded conductive plate a human hand, and if the other conductive plate is an electrode inside the sensor, we can then have a proximity sensing circuit, Fig. 1.4.

By replacing both the power source and the voltmeter with two digital pins in a microcontroller board (for example an Arduino), we can measure the transient time by sending a high digital signal to pin 1 and then count the time it takes for the signal to become high at pin 2. The transient time will be a function of the capacitance (C), resistance (R) and voltage (V). Higher resistance values will increase the transient time, allowing for more sensitive measurements at the expense of longer response times. Capacitance is dependent on the distance between the hand and the sensor, but it can no longer be determined by the parallel capacitor formula as a plethora of other variables become involved (skin conductivity, air humidity, interference from the surrounding environment, etc.). The voltage measurements are also dependent on the reference ground values, which may vary. This method is imprecise for distance measuring, but it enables a relatively reliable detection of the presence of humans in the surroundings and is easy to implement.

Chapter 2

Prototype Sensor

2.1 Design

Development of the proposed piezoresistive/self capacitive hybrid sensor was driven by different design goals:

1. Easy manufacturability at an affordable cost using common materials and tools.

2. Tactile resolution to detect human touch.

3. Sensible to forces of up to 15 N.

4. Detection of human presence at distances shorter than 100 mm.

5. The structure of the sensor should be flexible to adapt to different geometries so that it can be applied like masking tape. The sensors will be applied on the end-effector of an industrial collaborative robot or along the robot's arm.

We developed a sensor featuring an FSR array with 16 prexels of 48 mm^2 each, disposed in a 2 x 8 configuration. Only 25% of the total sensor area is effectively pressure sensitive. The remaining blind area can be reduced either by augmenting the number of prexels, or by using connected structure-based methods [61]. The area of each prexel should be approximately the area of the tip of a human finger (to detect hand or finger contact). Increasing the area beyond this point would reduce the sensor's accuracy, making it less suitable to fine robot-hand guiding. A final design consideration is related to the maximization of the area of the self-capacitive electrode to improve proximity detection. Maximum detectable distance should be in the order of the size of the electrode.
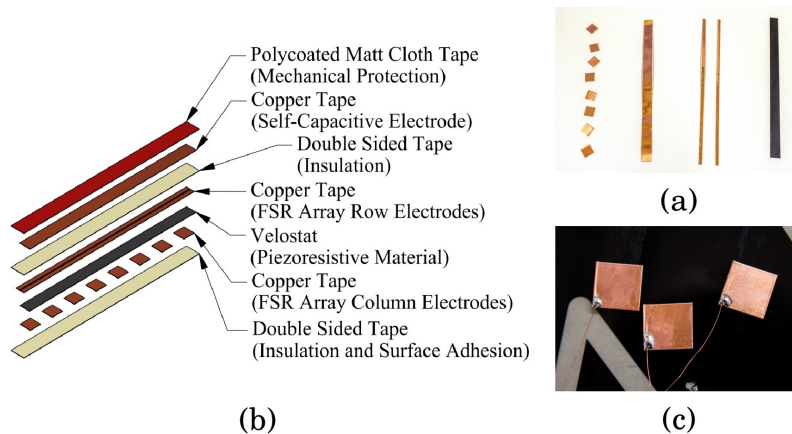
Figure 2.1: Sensor's internal elements. a) Exploded view of the sensor's elements; b) Copper electrodes and Velostat strip; c) Detail of solder connections.

2.2 Manufacturing

The manufacturing process of the sensor is composed of several steps leading to the assembly of all the sensor's elements, Fig. 2.1b. The main aspects of each manufacturing step are highlighted and discussed below:

1. Copper tape and Velostat pieces were cut according to the dimensions necessary for the sensor. These include 8 prexel column electrodes, 2 prexel row electrodes, 1 Velostat strip and 1 self-capacitive copper electrode, Fig. 2.1a. The manufacturing process should ensure that there is no contamination on the conductive surfaces.

2. Enameled copper wires were soldered to each copper electrode, Fig. 2.1c. It is important to avoid the flow of solder to areas that will be in direct contact with the semi-conductive polymer. Solder build-ups outside those areas should also be kept to the bare minimum, as they will create pressure concentration zones and promote layer separation, decreasing the sensor's low-pressure sensitivity through a sharp increase in the electrical contact resistance between layers. Finally, all copper parts were thoroughly cleaned with isopropyl alcohol, both before and after the soldering process.

(a) (b) (c) (d)

(e) (f) (g) (h)

(i) (j)
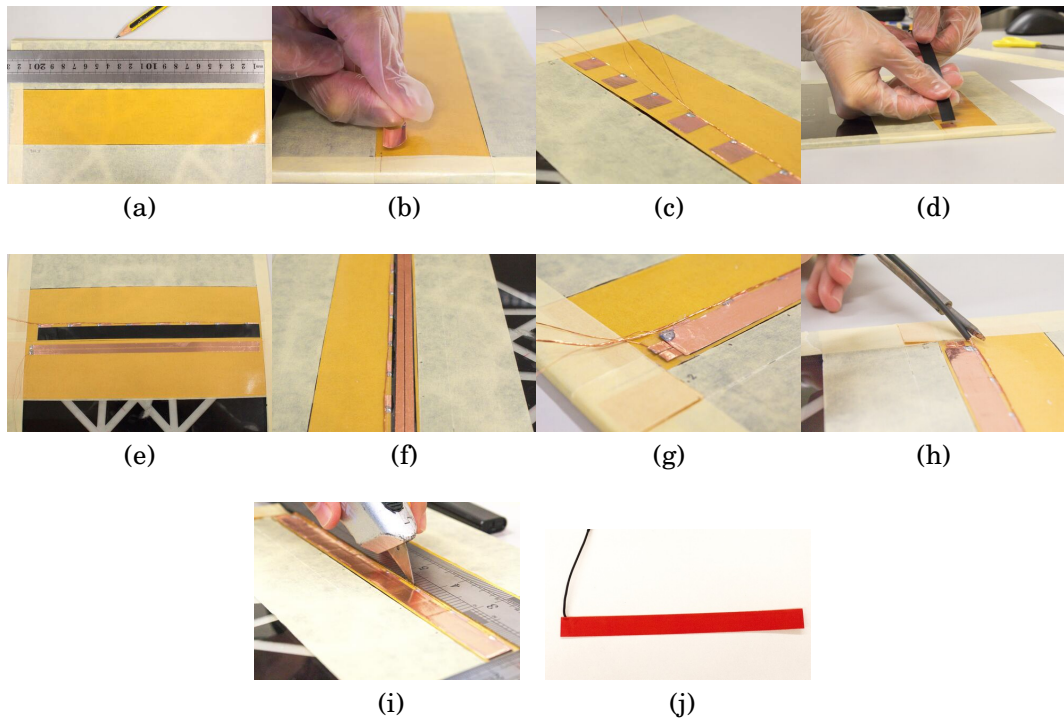
Figure 2.2: Sensor manufacturing process.

3. To make the sensor's base layer, a strip of double-sided tape was unrolled on top of a flat surface with its adhesive side up and held in place with strips of painter's tape. We used a pencil to mark the measurements, Fig. 2.2a. Later, we found this not to be recommended, due to the potential for contamination with graphite particles.

4. The 8 prexel column electrodes were glued to the base layer, Fig. 2.2b. Their enameled wires were twisted, Fig. 2.2c, and stuck to the base layer beneath. All wires must be inside the sensor's design dimensions.

5. The Velostat layer was laid on top of the 8 column electrodes, Fig. 2.2d. It is essential to ensure proper insertion at the first attempt. Unsticking and relocating the polymer can lead to adhesive residues finding their way to areas that will be in direct contact with the copper electrodes, affecting the electrical contact resistance between layers.

6. A second strip of double-sided tape was placed on the workbench with its uncovered sticky side up. This will be the sensor's middle

insulating layer, separating the row of the FSR array's electrodes from the self-capacitive electrode. After appropriate measurements, both rows of copper electrodes were glued in place, Fig. 2.2e.

7. The middle insulating layer, with the 2 rows of electrodes, was placed on top of the Velostat layer and the lower cover of the adhesive was removed, Fig. 2.2f.

8. The self-capacitive electrode was installed, and all wires were twisted together and arranged as flat as possible to reduce the risk of layer delamination, Fig. 2.2g. A heat shrink tube was installed to provide further insulation and surface protection to the enameled wires, Fig. 2.2h.

9. The sensor was cut to shape and covered with its final layer of poly-coated matt cloth tape which will provide surface protection, Fig. 2.2i. The fully assembled prototype is shown in Fig. 2.2j.

2.3 Data Acquisition System

The Data Acquisition System (DAQ) is composed of three main components:

1. A custom-made Arduino shield.

2. The Arduino itself, which runs the sensor's transfer functions and communicates with an external serial client.

3. An external computer, which receives and processes the sensor's data and interfaces with the robot's controller.

The shield, circuit in Fig. 2.3, is composed of two 3-bit multiplexers (ST Microelectronics M74HC4051B1) to address the column-row pairs in the FSR array. This enables a maximum array size of 64 prexels, disposed in an 8 x 8 configuration. Higher bit multiplexers will enable exponentially larger sensor arrays. We used a voltage divider circuit with a reference resistor of 1 kΩ to measure the electrical resistance of each prexel. This is a low value to use with FSRs, but this proved to be the average value of our sensor in the 5 to 10 N range, where the highest precision was required. A 1 MΩ resistor was used for the proximity sensing circuit. Although higher values would increase the sensitivity of the sensor, they also significantly increase signal noise. Some users of the Capacitive Sensing Library [5] for Arduino also report good signal noise reduction
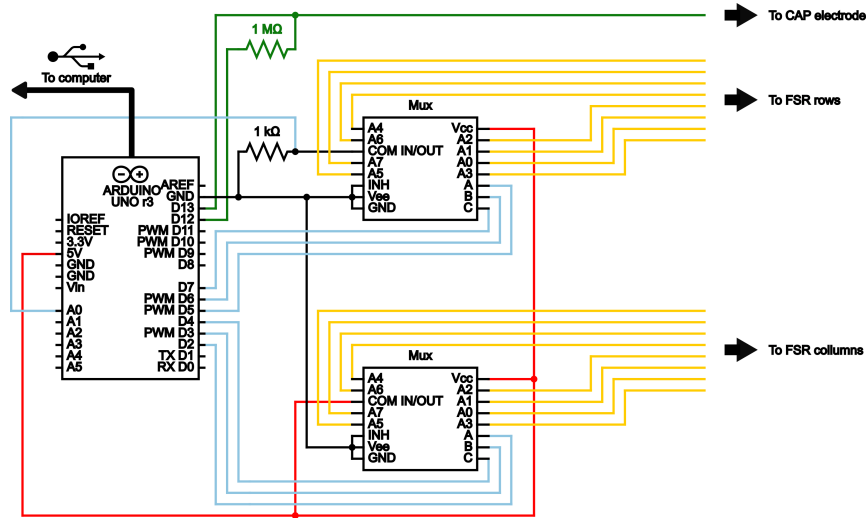
Figure 2.3: Data Acquisition System (DAQ) circuit diagram.

by the inclusion of a small capacitor between the sensor's self-capacitive electrode and ground reference voltage. We tested the inclusion of such capacitor in our circuit and the results proved to be relatively poor, as the sensitivity of the sensor seemed to decrease.

The Arduino (Uno version) was used to: (1) establish the connection to the serial client, (2) ask the client for the FSR array dimensions, (3) measure self-capacitance (apply the transfer function to determine approximate distance), (4) address multiplexers to connect each prexel in the FSR array (to measure prexel electrical resistance and apply the transfer function to determine the force applied), (5) send values to the serial client, and (6) return to point (3). The external computer receives serial data from the board using a MATLAB-based platform as it can simultaneously receive data from the Arduino and perform real-time robot motion control using the KUKA Sunrise Toolbox (KST) [47].

21

Chapter 3

Sensor Characterization and Experiments

A comprehensive theoretical approach for FSR modeling was proposed in [23]. However, it requires advanced material analysis techniques which may be inaccessible to some researchers. For that reason, we propose an empirical model based on polynomial regressions. The characterization of the self-capacitive proximity response was also achieved using an empirical model. It proved to be effective in detecting the presence of a human hand from up to 100 mm away. Table 3.1 details some of the main specifications and characteristics of the sensor.

3.1 FSR Empirical Model

3.1.1 Force-Electrical Resistance

The force-electrical resistance relationship was evaluated in a compression test stand we specifically designed and built, Fig. 3.1. It is composed of a rubber pressure test tip designed to closely resemble the effective area and pressure distribution of a human finger in contact with the sensor. In the first experiment, the sensor was subjected to forces ranging from 0 to 15 N in step increments of approximately 0.4 N. The resulting electrical resistances were recorded. The test was repeated 6 times at an average room temperature of 25ºC. Fig. 3.2a and Fig. 3.2b show both the resistance and conductance measurements, respectively.

Table 3.1: Sensor specifications and characteristics.

Parameter	Value
Size of tactile elements	4x12 mm^2
Thickness	1 mm
Minimal detectable force (resistive mode)	0.5 N
Single point repeatability (at 8.1 N)	11.3%
Static loading (after 3 hours)	6.1% relative to measured force
Drift (3 hours at a constant force of 8.1 N)	5.8% per log(min)
Presence detection	100 mm
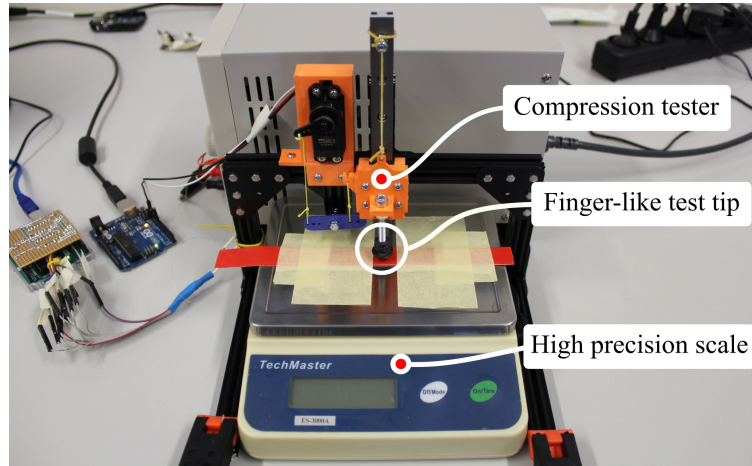
Figure 3.1: Experimental setup of the force-electrical resistance compression test.

(a) Measured force-electrical resistance.

(b) Measured force-electrical conductance.

(c) FSR array model with 95% confidence intervals (force-conductance).
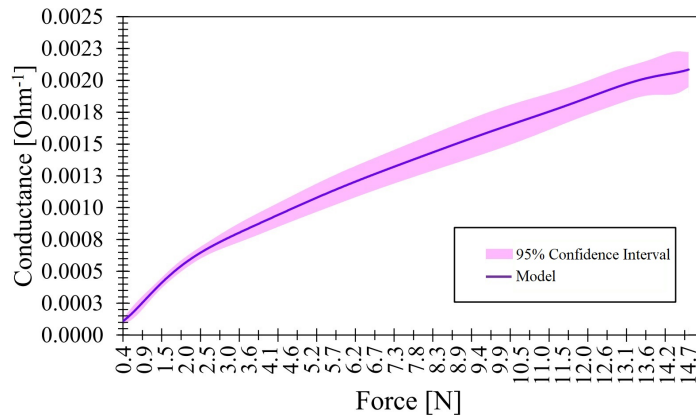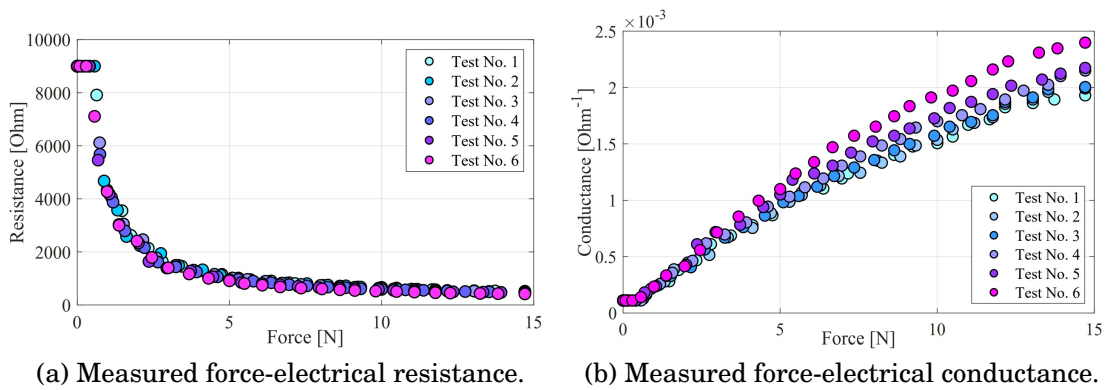
Figure 3.2: Sensor response.

Force-conductance data show a linear behavior, so that it can be subjected to linear regression to obtain the desired empirical model. However, there are some pointwise exceptions consistent to all 6 recorded data sets. These deviations occur mainly due to the layer deformation caused by the copper connections inside the sensor. To take these deviations into account, high degree polynomial regressions can be considered to better fit the force-conductance data. Choosing between linear and higher degree regressions is a balance between better response times or higher precision. Also, as expected, the sensor proved to be inaccurate when subjected to forces lower than 0.5 N. This is mainly due to the delamination phenomena. Small pockets of air get between the semi-conductive polymer and the electrodes inside the sensor, creating an unpredictable increase in the electrical contact resistance between layers, and which makes precise force measurements difficult. We did not take these low
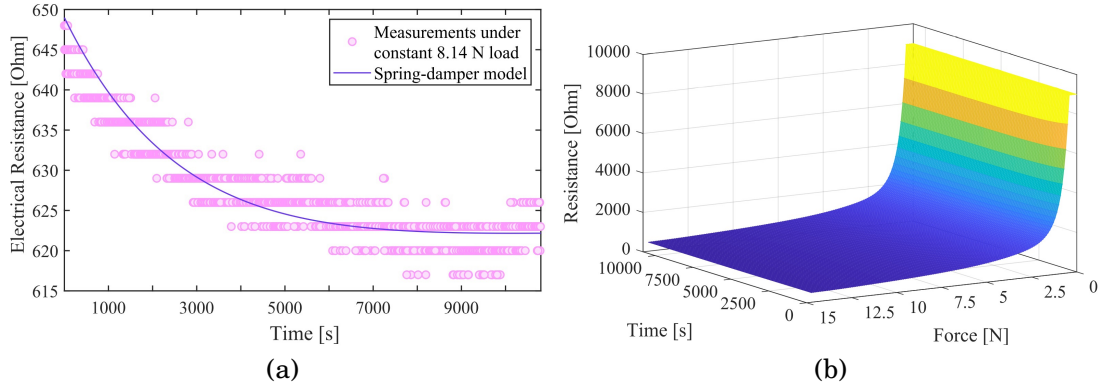
Figure 3.3: a) Signal drift and spring-damper model. b) Three-dimensional FSR model considering stress relaxation.

force/conductance values into consideration when performing the regressions, as they present an unpredictable behavior and would have polluted our model with non-significant data. For our specific model, a high degree polynomial was fitted to the average force-conductance values across all 6 tests, and the standard deviations for each point were calculated. Confidence intervals of 95% were calculated assuming multiple measures of the same force follow a normal distribution, Fig. 3.2c.

3.1.2 Signal Drift

In a second experiment, a constant force was applied during a 3-hour test, to determine the sensor's signal drift. The data resulting from this test show an asymptotic decrease in electrical resistance over time, Fig. 3.3a. Velostat's electrical resistance is mostly a function of the material's strain. The graph in Fig. 3.3a shows a behavior that is similar to the Stress-Time graph of a viscoelastic material undergoing stress relaxation. This behavior can be modelled by a spring-damper system. According to the laws of mechanical vibrations, the position of such a system, when critically damped, can be described by Eq. 3.1,

$$x(t) = (x_0 + (\mathring{x}_0 + \omega_n x_0) \times t) \times e^{-\omega_n t} \qquad (3.1)$$

where x_0 is the system's initial position, $\mathring{x}_0$ is the system's initial velocity and ω_n is the system's natural angular frequency. Adapting Eq. 3.1 to model the signal drift of our sensor, we have:

$$R(t) = (\Delta R + (A + B\Delta R) \times t) \times e^{-Bt} + R_0 - \Delta R \qquad (3.2)$$

where R_0 is the initial electrical resistance, ΔR is the difference between the initial and final electrical resistance measured, A and B are parameters that can be determined by a numeric method. We used a curve fitting method combining the previous force-resistance and resistance-time models, so that we can finally generate a complete empirical model, Fig. 3.3b.

3.2 Characterization of the Self-Capacitive Proximity Response

The sensor proved reasonably effective at detecting the presence of a human hand up to 100 mm away. Since it is hybrid, featuring both FSR and self-capacitive modes, it could easily distinguish between the touch and the presence of a hand in its surroundings. A purely empirical model was used to model the sensor's proximity response. Three experiments were conducted to evaluate its effectiveness.

In the first experiment, the sensor was put on top of a non-conductive surface without any objects in close proximity. Proximity data obtained from the Capacitive Sensing Library were recorded to determine the system's base value which would serve as a control reference value. The base value recorded was an average digital value of 1486, with a standard deviation of 29.

In the second experiment, a human hand gradually approached the sensor until physical contact was established. The reference distances between the hand and the sensor were: 400 mm, 350 mm, 300 mm, 250 mm, 200 mm, 150 mm, 100 mm, 75 mm, 50 mm, 25 mm, 10 mm and 0 mm. After physical contact was made, three different scenarios were considered and the data recorded: 1) the hand resting on the sensor's surface, 2) a single finger resting on the surface, and 3) a single finger pressing on the surface. The results in Fig. 3.4 show a high level of data dispersion (difference in minimum to maximum values), which makes it essential to employ signal filtering to infer hand to sensor distance. We implemented a moving average filter, with relative success, at the expense of system response time. As expected, the system's spatial resolution is very low (30 to 50 mm) and the detection of a presence is only reliable at distances shorter than 100 mm. The response curves in Fig. 3.4 can be fitted by a rational equation.
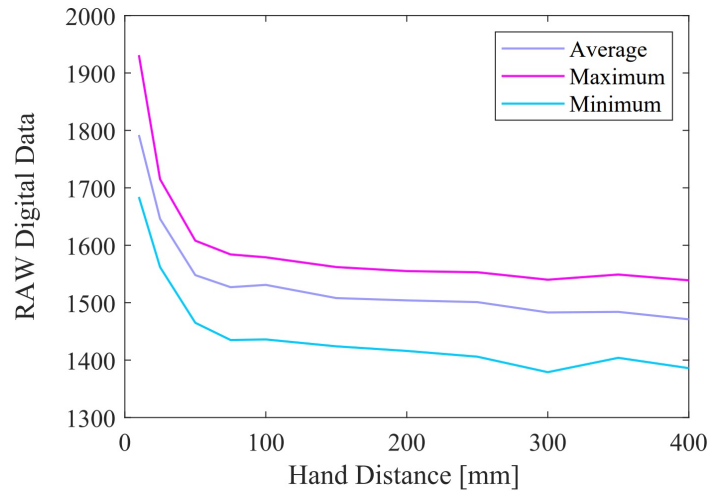
Figure 3.4: Detection of a human hand at different distances from the sensor.

The third experiment was similar to the second experiment, but instead of having a human hand approaching the sensor we had an object: a small anodized aluminum rod; an aluminum caliper; a steel hammer and a 500 ml plastic water bottle (full). The sensor could not reliably detect the presence of any of these objects. Although this represents a limitation to the sensor, it can be seen as an advantage as it makes it possible to distinguish between the proximity of a hand from objects clearly. This advantage is important in robotic applications, where we need to know if the objects close to the robot are humans or objects/equipment.

Chapter 4

Application in Real Robotic Systems

Having made and characterized the proposed sensor, we applied it in two distinct robotic case studies: guiding of a robot by hand (measuring touch force and hand proximity) and human-robot collision avoidance (measuring hand proximity). The sensor, owing to its flexibility, was installed around the robot end-effector as if it was masking tape, Fig. 4.1. The collaborative robot is a 7 DOF KUKA iiwa R800 equipped with the Sunrise controller and interfaced using the KST Toolbox [47]. For both applications it is necessary to acquire data from the sensor at 50 Hz, otherwise the robot will not present a smooth behavior while being hand-guided or avoiding collisions.

4.1   Hand Guiding the Robot

For the robot hand-guiding application, force-sensing measurements are acquired, treated and transformed into robot motion commands, i.e., translations in Cartesian space. Proximity sensing, which is also used in the collision avoidance experiments, covers safety functions, namely the detection of the human hand to slow down robot motion to trigger the robot hand-guiding control mode.

As indicated before, the sensor has 16 prexels disposed in a 2 x 8 FSR array, 2 lines (A and B) and 8 columns (1, 2, ..., 8), Fig. 4.1a. Each one of the columns of the array, when touched, triggers a corresponding robot motion in x-y Cartesian space. Motion direction is defined by the calibration of the sensor with the robot end-effector reference frame. When the sensor is touched, the robot's motion is directly mapped from the forces measured at each column of the array of prexels. When a given pressure

(a)   (b)
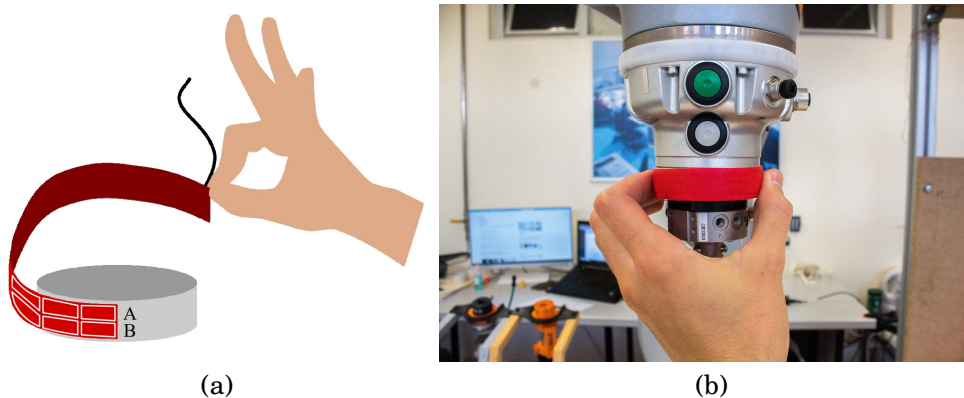
Figure 4.1: a) Hand guiding of robot manipulator. b) Installation of the sensor on the robot's flange.
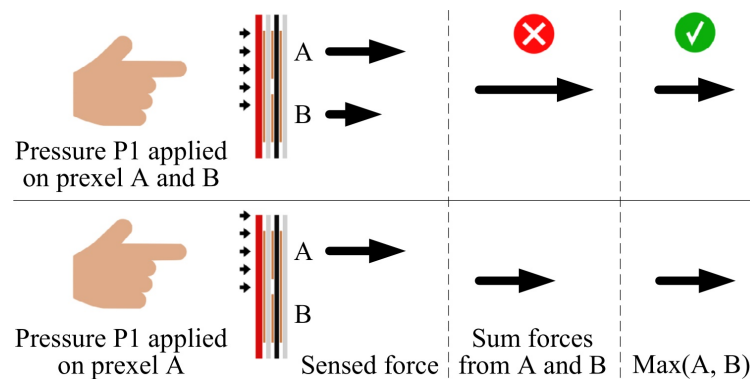
Figure 4.2: Forces measured in a column of prexels.

is applied to the sensor, depending on the exact position of the finger, that pressure might be spread to either one or both prexels in the column (A and B), Fig. 4.2. Only the maximum column force, applied to prexel A or prexel B, is considered. Otherwise, adding the measured forces sensed across both columns of prexels would result in overmeasurements. The sensor's design guarantees that at least one of the two prexels in each column is fully covered by the human finger.

To hand guide the robot along the z-axis, we calculated the pressure differential between both prexels in each column of sensors. The sensor's width (column height) is approximately the size of a finger touching the sensor. The human finger tends to touch the sensor in the center (the sensor's dimensions force that scenario), leading to an approximately equal pressure distribution between the prexels in the top and lower rows. When a human tries to push the robot upwards, or downwards, an angular momentum is created between the skin's surface (where a trac-
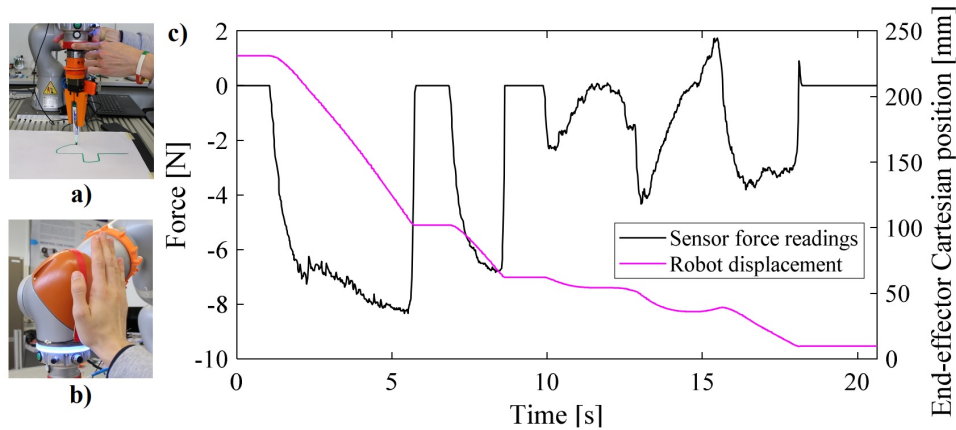
Figure 4.3: a) The robot is hand-guided using force measurements from the sensor, b) the robot moves to a safe position when it detects the proximity of a human hand using proximity measurements from the sensor, c) robot end-effector Cartesian displacement in relation to hand-guiding forces measured by the proposed hybrid sensor.

tion reaction force is applied to the sensor's surface) and the bone inside. This momentum causes a natural deformation of the finger, which in turn changes the balance of pressures between both rows of FSRs. The pressures measured indicate the intention of the human to move the robot end-effector along the z axis (upwards or downwards). Another solution would be to use extra sensors placed on the robot's structure to move it accordingly.

According to the forces sensed, the robot's motion is controlled by directly mapping the magnitude of the forces and the direction of the robot's motion, Fig. 4.3. Different users indicated that the hand-guiding process is natural, as they can intuitively move the robot at the end-effector level.

4.2 Avoidance of Human-Robot Collision

In order to avoid human-robot collision effectively, the proximity of the hand to the robot must be measured using the self-capacitive characteristics of the sensor. As the sensor detects the human hand, we associated the distance to the robot with robot motion commands that make it move to a safe home position. As the hand approaches the sensor, the speed of the robot's movement towards the safe position increases, Fig. 4.3. The

detection of the human hand was demonstrated effectively since the robot reacts by moving away from the hand to a safe home position smoothly.

Chapter 5

Conclusion and Future Work

In Part 1 of this thesis we presented a novel mechanically flexible piezoresistive and self-capacitive hybrid force and proximity sensor, which proved to be: efficient, reliable, multifunctional, easy to fabricate, low cost and as easy to apply as masking tape. These characteristics demonstrated its potential application not only in robotics but also in several other fields (smart home devices, machine interfaces, etc.). The experimental results, for both the force-electrical resistance and self capacitive proximity response showed the sensor's versatility, flexibility (1 mm thickness), accuracy (reduced drift) and repeatability. The proposed fabrication method was shown to be flexible enough to accept process variations. The sensor was successfully applied for use in hand guiding a robot and the avoidance of collisions. Future work will be dedicated to testing other manufacturing processes to reduce the electrical contact resistance between layers.

Part II

Untethered Phase Change Artificial Muscles

Chapter 6

Motivation and Basic Principles

6.1 Introduction

Bioinspired soft material actuators have unique characteristics that make them suitable for a number of promising applications [53]. The inspiration in biology led us towards robots that are compliant as animals' soft tissues and muscles, especially when interacting with unstructured environments [42], [65], adjusting behavior in a flexible manner due to its intrinsic material compliance. Such behavior is hard to achieve when robots only rely on rigid materials. In fact, soft robots increasingly present new abilities related to their design, modeling, fabrication and control [26]. These intrinsic characteristics (compliance, low weight, versatility and high actuation speeds) of soft robotics make them well suited to safe interaction with humans, even in the presence of contact with humans [7]. Soft actuators artificial muscles will shape the next generation of robots, achieving the functionalities of biological systems [45]. Nevertheless, existing soft robotic systems still lack in versatility, mobility, output force, performance, and reliability when compared to biological muscles. Their applications span the most diverse domains, from medical, to industry, to aerospace [43].

Soft mechanisms are challenging to actuate and control, namely the stiffness control [2]. Traditionally, it can be done by controlling the pressure (inflate and deflate) inside the soft system using pneumatic actuation. When inflated the soft system deforms according to its design. The McKibben artificial muscle is a representative and well-known example of a soft actuator which still today serves as inspiration for many soft mechanisms [25]. Its design forces the radial expansion of the structure

34

when pressurized. McKibben pneumatic muscle actuators demonstrated effectiveness performing movements requiring large instantaneous forces with short duration [38].

6.2   Related Work

Recently, researchers investigated actuation by vaporizing embedded liquid (ethanol) in the soft mechanism using ultrasonic waves to excite it and inflate the soft structure [27]. This method has pros and cons in relation to boiling. The pros are that is faster and the process occurs at lower temperatures. The cons are the use of ethanol and the required apparatus to set up the ultrasonic waves. These are techniques toward untethered robotic actuators, which are fundamental for robotic applications featuring robot autonomy and availability (without being constrained by the power source) [44]. A new soft mechanism design featuring relatively high speed and manipulation strength was recently presented [55]. The proposed design leverages tunable snap-through bistability so that soft robots rapidly store and release energy within tens of milliseconds. Within this technology, different actuation methods and materials may be used.

The liquid-vapor phase transition of ethanol and a phase-change material confined within an elastomer matrix has been used for the development of a programmable soft actuator based on volume expansion/retraction [24]. The actuator is controlled by changing the ethanol temperature, above or below the boiling point. It demonstrated good bending at temperatures higher than 90 ºC, easy to automate and able to operate underwater. On the other hand, the response time is relatively slow and the manufacturing process introduces some relative complexity. In an interesting study, researchers proposed a soft system with small pores filled with ethanol where a resistive wire was used to increase the temperature [32]. Power can be wirelessly transferred to an inductor-capacitor resonator that heated and vaporized a low boiling point liquid [8]. Untethered soft actuators, composed of self-contained liquids and super-elastic chambers, featuring liquid to vapor transition using near-infrared light have been proposed [17]. With volume change in chambers, the actuator reaches up to 160% in elongation and an output force of 14.5 N with 6 g self-weight. Its fabrication and control can be considered relatively challenging. Möbius strip actuators using a photothermally responsive liquid crystal elastomer are actuated by light [37]. Another light-driven soft device, made of a light-responsive liquid-crystal elastomer that senses the environment and acts as a power source, uses optical feedback to trigger

photomechanical actuation [62]. Inspired on plants, a reversible osmotic method was proposed to actuate a tendril-like soft robot [34]. It is based on the electrosorption of ions on flexible porous carbon electrodes driven at low input voltages.

Twisted-and-coiled actuators, driven by electricity, are promising for actuating centimeter-scale soft robots, being able to deliver 48% free strokes (contraction without preloading) [54]. Taking advantage from the nematic-isotropic phase transition of liquid crystal mesogens, liquid crystal elastomer microfibers can generate large actuation strain (~60%) with a fast response speed (<0.2 second) and a high-power density (400 Watts per kilogram) [18].

Multimaterial 3D printing was used to manufacture an untethered combustion-powered robot driven by butane and oxygen [6]. The transitions from rigid to soft are based on a stiffness gradient interface. However, they are difficult to control. Multimaterial 3D printing technologies demonstrated feasible the fabrication of an anthropomorphic skeleton hand that shows anisotropic mechanical stiffness [21]. Recently, it was demonstrated the design and fabrication of voxelated soft matter using multimaterial multinozzle 3D printing [50]. This method was demonstrated to be effective for the fabrication of complex designs. Recently, soft pneumatic actuators have been fabricated using Rapid Liquid Printing (RLP), offering design freedom in relation to traditional silicone casting and additive manufacturing of elastomers [52].

Various designs of hydraulically amplified self-healing electrostatic (HASEL) actuators with muscle-like performance have been proposed [1]. Electric fields displace liquid dielectrics enclosed in soft hydraulic bodies, reducing losses in speed and efficiency associated with transporting fluid through channels. These actuators combine the versatility of soft fluidic actuators with the muscle-like performance of dielectric elastomer actuators (DEAs) to achieve linear strains exceeding 100% and a relatively high-speed operation. On the other hand, its fabrication requires flexible conductors and its actuation is on the kilovolts range which may bring some safety issues when operating close to humans. The HASEL actuator demonstrated the ability to create an untethered continuum robot for grasping and manipulating delicate objects [33]. In what concerns to the portability a lightweight, flexible, electro-pneumatic pump is proposed to control volume and pressure of an untethered soft robot actuator [13]. The actuation relies on a dielectric fluid-amplified electrostatic zipping, achieving pressures of 2.34 kilopascals and deliver volumetric flow rates up to 161 milliliters per minute and under 0.5 Watts of power with a thickness of 1.1 millimeters and weight of 5.3 grams. This solution demonstrated to be able to drive a soft actuator to achieve a maximum

contraction change of 32.4% and actuation velocity of 54.4% per second.

Untethered soft robotics, while having enormous advantages, bring several scientific challenges [44]. Traditional soft actuators use a supply of pressurized fluid (usually air supplied by pneumatic tethers) to drive the shape change through the deformation of the soft body (usually flexible or stretchable polymers). Typically, they are tethered to a source of pressurized fluid, requiring diverse channels and tubes, which is a limitation in what concerns to portability, design and fabrication. In the last two decades, dielectric elastomer actuators (DEAs) demonstrated to achieve high actuation strain, high-speed operation and self-sensing capabilities [41]. On the other hand, they are vulnerable to failure due to dielectric breakdown and require stretchable materials for their fabrication (for both electrodes and dielectric layers). Inspired by living organisms, untethered millirobots with multiple tapered soft feet architecture have been developed [28]. They demonstrated the ability to adapt to harsh environments with high locomotion efficiency, carrying capacity and obstacle avoidance.

6.3 Concept

Virtually every pneumatic soft actuator consists of some sort of flexible inflatable bladder, which deforms producing work when inflated. In the case of McKibben Pneumatic Artificial Muscles (PAM), the flexible bladder is a cylindrical tube shrouded by a braided sleeve made of non-extensible threads. Inflation of the inner bladder causes an increase in volume, which is constrained by the sleeve leading to longitudinal contraction or extension, depending on the specific characteristics of the braid being used.

Our proposed actuator, illustrated in Fig. 6.1, adds two main elements to the traditional pneumatic McKibben actuator: an electric heating element, and a work fluid.

The underlying principle is simple: use electric energy to heat and boil the work fluid in order to provide the pressurization necessary for the desired deformation. This will be referred to as a Phase Change Artificial Muscle (PCAM).
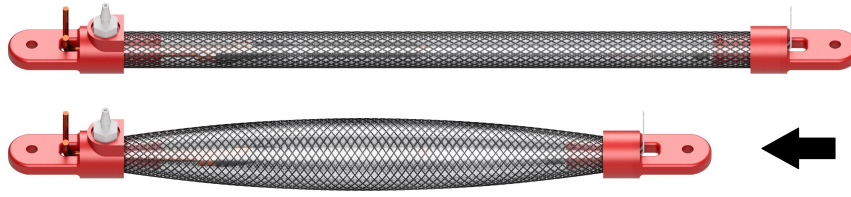
Figure 6.1: Electrically powered Phase Change Artificial Muscle (PCAM).

(a) Subcooled   (b) Saturated
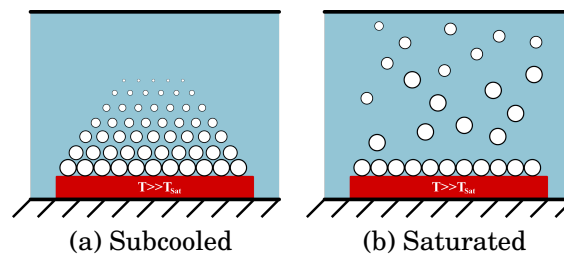
Figure 6.2: Pool boiling.

6.4 Liquid-Gas Phase Change

Inside the actuator, a work fluid is subjected to what is known as pool boiling: a form of convection heat transfer in which a liquid, void of bulk motion, is exposed to a hot surface whose temperature exceeds the saturation temperature of the liquid (T_{sat}). Vapor bubbles first nucleate on the solid-liquid interface, increasing in size until they eventually detach, rising towards the surface. These bubbles – usually not in thermodynamic equilibrium with the adjacent liquid – allow for transfer of heat between the two phases. If the temperature of the adjacent liquid is significantly lower than its T_{sat}, vapor bubbles tend to collapse before they reach the liquid's free surface – a process known as subcooled pool boiling. On the other hand, when the temperature of the liquid gets sufficiently close to T_{sat}, vapor bubbles manage to rise all the way to the surface. This is known as saturated pool boiling.

The collapse of vapor bubbles during subcooled pool boiling is similar to the phenomena of cavitation: the first being caused by a localized increase in temperature; the second by a local decrease in pressure. Both result in a successive collapse of bubbles which generate high-frequency shockwaves that spread throughout the liquid medium. The impact of these shock waves on the internal elements of the actuator – particularly

the heating element and monitoring sensors – proved to be a source of concern and will be further discussed in Chapter 8.

6.5 Work Fluid

The work fluid's basic function is to allow the conversion of heat energy (Q) into work energy (W). The energy required to vaporize a unit mass of liquid fluid – its specific enthalpy of vaporization (ΔH_{vap}) – is defined by Eq. 6.1 [51].

$$\Delta H_{vap} = \Delta U_{vap} + \Delta(PV) \tag{6.1}$$

where ΔU_{vap} is the change in specific internal energy of the fluid undergoing vaporization, P its absolute pressure and V its specific volume.

From the total invested energy (ΔH_{vap}), a portion will be converted and returned by the fluid to the environment in the form of work ($\Delta(PV)$). This is the energy which can be made useful. The rest (ΔU_{vap}) will later be released as heat during the opposite phase transition (condensation), and dissipated away unless some kind of regenerative cycle is used.

We may then consider the quotient $|\Delta(PV)/\Delta H_{vap}|$ or, in other words, the work fraction $|W/Q|$ as the maximum theoretical efficiency of non-regenerative phase change actuators undergoing isobaric expansion.

As an example, consider 1 kg of saturated water being vaporized at constant atmospheric pressure. From the total invested energy ($Q = \Delta H_{vap} = 2256,9$ kJ), approximately 92,5% is absorbed ($\Delta U = 2087.5$ kJ) while the remaining 7.5% is returned in the form of work ($W = $ -169.4 kJ). If the actuator was otherwise ideal with no further losses, its efficiency would thus be 7.5%.

We started by calculating this parameter over a wide range of saturation pressures ranging from 101.33 kPa (standard atmospheric pressure), up to more than 250 kPa, for most work fluids commonly proposed in phase-change soft actuators. Results are seen in Fig. 6.3, and the calculation procedure is shown in detail in Support Material 01.

Water presents a relatively low $|W/Q|$ quotient, ranging from the aforementioned 7,5% at atmospheric pressure, up to approximately 8.2% at 230 kPa which we will consider the maximum safe operating pressure for
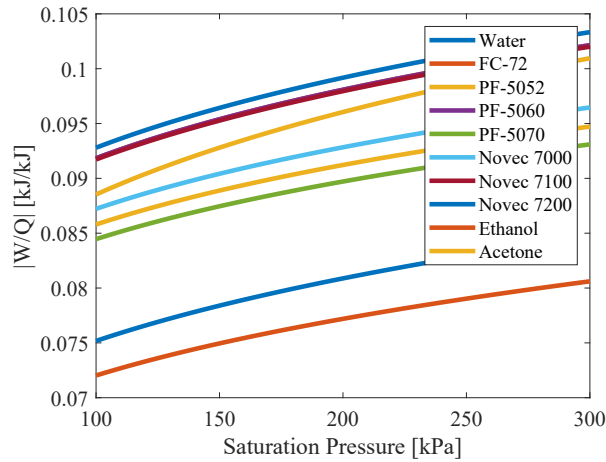
Figure 6.3: Work/Heat quotient during isobaric liquid-gas phase transition.

our actuator. In comparison, ethanol, one of the first work fluids to be implemented in a phase change soft actuator by Miriyev et al. [32], presents an even lower $|W/Q|$ quotient of 7.2% at atmospheric pressure, and 7.8% at 230 kPa. Higashijima et al. [19] presented a small phase change pressurization unit for use with traditional McKibben actuators, using 3M's Fluorinert PF-5052 fluid, which has a significantly higher $|W/Q|$ quotient ranging from 8.6% to 9.2% between the same pressures. Recent work by Narumi et al. [35] demonstrated another type of phase change-based soft actuator – a Liquid Pouch Motor – using 3M's Novec 7000. Of all the fluids analyzed, the theoretically most efficient would be 3M's Novec 7200, reaching a $|W/Q|$ of 10% at 230 kPa absolute. No previous work was found using this fluid.

Other important factors to consider when selecting work fluids for soft actuators are:

- Boiling point

- Chemical compatibility

- Safety and toxicity

Fluids with lower boiling points usually allow for lower operating temperatures, which may be essential to guarantee operational safety. It is also worth noting that, to avoid significant response lag, the actuator should be kept in a preheated state with its fluid in saturated liquid form while awaiting commands. Lower operating temperatures reduce the rate of heat being dissipated through natural convection while the actuator is

Table 6.1: Comparison between popular work fluids.

Fluid	Boiling Point (@ 1 atm) [ºC]	Enthalpy of Vaporization (@ 1 atm) [kJ/kg]	Liquid Specific Heat [J/kg.K]	Flammable	Flash Point [ºC]	Autoignition Temperature [ºC]
Fluorinert FC-72	56	88	1100	No	-	-
PF-5052	50	105	1050	No	-	-
PF-5060	56	88	1050	No	-	-
PF-5070	80	80	1050	No	-	-
Novec 7000	34	142	1300	No	-	-
Novec 7100	61	112	1183	No	-	-
Novec 7200	76	119	1220	No	-	-
Ethanol	78	838.3	2560	Yes	13	455
Acetone	56	538	2140	Yes	-17	465
Water	100	2257	4180	No	-	-

preheated, improving its overall efficiency. However, one factor usually neglected by authors is that these lower heat dissipation rates promote lower condensation rates during actuator depressurization. This limiting factor on depressurization rate will be shown to be vastly more restrictive than the main limiting factor for pressurization rate – the Critical Heat Flux (CHF) – making the actuator necessarily slower to complete a full cycle.

Chemical compatibility must also be assured between the fluid and the wet elements of the actuator. The Novec series of engineering fluids are marketed as tube swellers by 3M themselves [1]. As mentioned by the manufacturer, Novec fluids are particularly effective at swelling a variety of materials including silicones and natural rubber (the latter with only minor swelling). Furthermore, the manufacturer also notes that fluid absorption by the elastomer may be followed by fluid loss through diffusion [2]. Such swelling and subsequent loss of fluid in soft phase change actuators was already reported by Garrad et al. [14].

Finally, fluid safety and acute toxicity were considered. Relevant parameters are presented in Tab. 6.2. According to the United Nation's Globally

---

[1]Novec Engineered Fluids - Tube Swelling, 2019 [Online]. Available: https://multimedia.3m.com/mws/media/1702683O/3m-tube-swelling-bulletin.pdf

[2]Novec Engineered Fluids - Performance, sustainability, safety. 2017 [Online]. Available: https://multimedia.3m.com/mws/media/1463476O/3m-novec-engineered-fluids-white-paper-for-thermal-management-fv-pdf.pdf

Table 6.2: Median Lethal Dose (LD50); Median Lethal Concentration (LC50) and symptoms of exposure.

| | Symptoms of exposure | | | Acute Toxicity | | |
| | | | | LD50 | LC50 | LD50 |
Fluid	Skin	Eye	Oral	Oral (rat)	Inhalation (rat, during 4h)	Dermal (rat)
Fluorinert FC-72	No	No	Very Low	>5000mg/kg	>276mg/l	>5000mg/kg
PF-5052	No	x	x	>5000mg/kg	>15.4mg/l	>5000mg/kg
PF-5060	No	No	No	>5000mg/kg	>276mg/l	>5000mg/kg
PF-5070	Minimal	No	No	x	x	x
Novec 7000	x	x	x	>2000mg/kg	820mg/l	>5000mg/kg
Novec 7100	Minimal	No	No	>5000mg/kg	>1000mg/l	>5000mg/kg
Novec 7200	No	Minimal	No	>2000mg/kg	989mg/l	>2000mg/kg
Ethanol	x	x	x	10.47mg/kg	124.7mg/l	x
Acetone	Dryness	Serious Irritation	Drowsiness	5.8mg/kg	76mg/l	x
Water	No	No	No	x	x	x

Harmonized System of Classification and Labelling of Chemicals (GHS) [58], a Median Lethal Dose (LD50) through oral exposure of between 5 and 50 mg/kg corresponds to an acute toxicity hazard of category 2 – fatal if swallowed – which is the case with both acetone and ethanol. The least toxic fluid is water, followed by Novec 7100, PF-5070 and Fluorinert FC-72.

Acetone and ethanol are both flammable and present flash points below room temperature (Tab. 6.1), making them a considerable fire hazard in the event of a leak. Water may eventually present an explosion hazard if electrolysis and subsequent accumulation of hydrogen and oxygen are allowed to occur. This will be further discussed in the Experimental Results section of this thesis.

Considering the aforementioned points, we selected water as the work fluid for our actuator mainly due to its high material compatibility, low cost, high availability, and minimal toxicity.

Chapter 7

Prototype Actuator

7.1 Materials

Each actuator is composed of 6 main elements: (1) End terminals, (2) Heating element, (3) Working fluid, (4) Inflatable bladder, (5) Braided sleeve, (6) Pressure Sensor.

The end terminals were 3D printed using a semiflexible thermoplastic polyurethane filament (TPU 98A from RS PRO). Besides having an adequately high softening point of 138 ºC, this filament supports relatively low printing temperatures (235 ºC) and may be used without a heated print bed, making it suitable for the vast majority of commercially available FDM 3D Printers.

The heating element is composed of 0.35 mm diameter FeCrAl wire (Kanthal A from Kanthal) arranged in a coil configuration. FeCrAl has a higher electrical resistivity when compared to other common alloys (such as NiCr, NiFe, or CuNi), enabling the actuator to work with lower currents for a given power and heating element geometry. Although NiCr alloys present better wet corrosion resistance, the aluminum oxide (Al_2O_3) formed on FeCrAl adheres better to the alloy's surface and is a better electrical insulator, when compared to chromium oxide (Cr_2O_3) formed on NiCr.

For the inflatable bladder, 4 different materials were selected and tested: natural rubber latex (6x9 mm Latex Amber Tubing from StonyLab), and three different platinum-catalyzed two-part silicone rubbers (EcoFlex 00-30; EcoFlex 00-50 and Smooth-Sil 940, all from Smooth-On). To provide meaningful comparisons between different materials, all silicone bladders were fabricated to the same dimensions as the latex bladder which came pre-formed as a 6x9 mm tube.

A braided PET sleeve (article. no. 06240405010 from SES Sterling) was
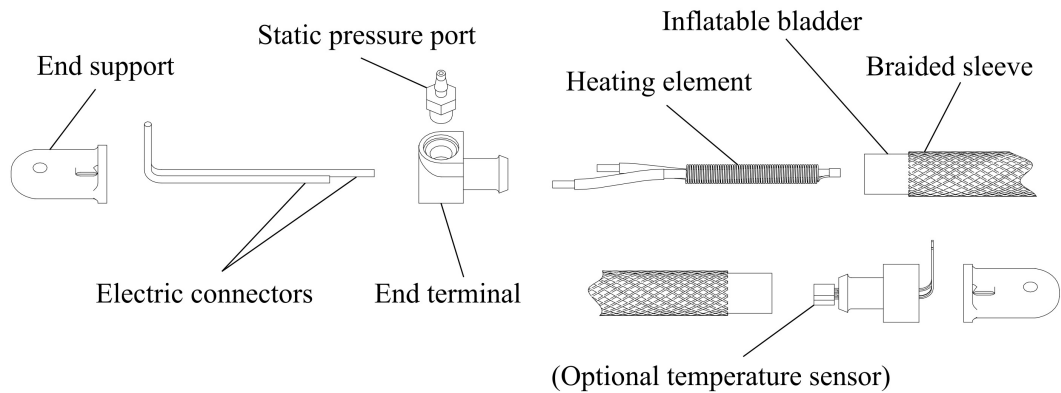
Figure 7.1: Actuator exploded view.

selected due to its low internal friction and relatively low thermal conductivity (compared, for example, to copper sleeves), which makes the actuator safe to touch even at higher operating temperatures, at the expense of slower relaxation speeds.

7.2 Actuator Design

7.2.1 Inflatable Bladder

As previously mentioned, all four inflatable bladders consisted of cylindrical tubes with 6mm internal and 9 mm external diameters. A lower tube length limit of 150 mm (+ 20 mm for fitting to end terminals) was calculated to ensure the heating element is entirely submerged in liquid fluid (with the actuator vertically mounted), when operating at its maximum design absolute pressure of 230 kPa at 10% strain. The calculation procedure is shown in detail in Support Material 02. Longer tube lengths allow for higher linear displacement, while shorter lengths may expose the heating element to the gaseous phase, resulting in a drastic increase in surface temperature due to the higher solid-gas convection thermal resistance. We opted for the minimum length of 150 mm, although early latex-based prototypes were also tested in 100 mm and 200 mm variants.

(a) 1x1 Biaxial   (b) 2x2 Biaxial

(c) 3x3 Biaxial   (d) Triaxial
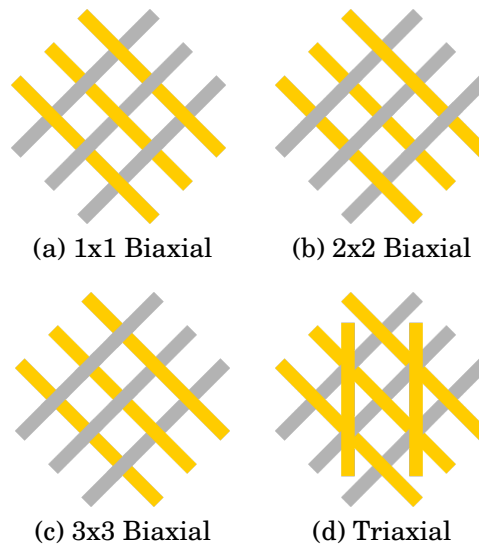
Figure 7.2: 2D schematic drawing of common braid unit cells.

7.2.2 Braided Sleeve

Most commercially available braided sleeves, in particular those made for the electronic and aerospace industries, follow one of the four braiding patterns presented in Fig. 7.2. Triaxial braids are usually non-extensible, as some of their yarns run parallel to their longitudinal axis. This makes them unsuitable for our application. The other three patterns are all biaxial braids, the difference being the sequence of yarns going over and under each other at subsequent crosspoints. The lesser curvilinear trajectory for each yarn is found in the 3x3 braid, which leads us to assume less energy would be dissipated as heat due to strain when its yarns slide across each other (when compared with the other two biaxial braids).

Friction between braid yarns can be experimentally modeled [10, 56]. More recently Davis and Caldwell [11] presented a theoretical friction model based on the Hertzian Contact Theory, although none has referred to potential differences between 1x1, 2x2 and 3x3 braids.

Our actuator's displacement will be directly related to the braid's own extensibility (ie. maximum longitudinal displacement), so it is also useful to understand how this can be affected by different braid parameters. Approximating the path of each yarn to a cylindrical helix (ie. ignoring the weaving curvature around crosspoints), the total braid length (L) can be determined by Eq. 7.1,

$$L = b \times cos(\theta) \tag{7.1}$$

where b is the length of each yarn and θ is the braid angle formed between each yarn and the braid's longitudinal axis (Fig. 7.3).

Since yarn length is a fixed parameter of a given braid, longitudinal extensibility may be approximated solely by determining the upper and lower limits of the variable braid angle.

The longitudinal force done by the braid, when subjected to an internal pressure can be approximated by Eq. 7.2 [10], assuming the braid remains cylindrical and without considering internal friction.

$$F = \frac{Pb^2}{4\pi n^2}(3 \times cos^2(\theta) - 1) \tag{7.2}$$

where P is the relative pressure acting on the inner side of the braid and n is the number of turns each yarn makes around the braid's longitudinal axis.

Solving Eq. 7.2 for θ when $F = 0$ results in a first positive root of 54.7º, known as the "neutral angle". This represents a theoretical upper limit for our braid angle during actuator contraction, and is independent of other braid parameters.

A lower limit can also be approximated by analyzing the fraction of area covered by the braid – known as *Cover Factor* (CF) – which can be calculated through Eq. 7.3, whose deduction is presented on Support Material 03.

$$CF = 1 - (1 - \frac{n \times W_y \times N_y}{b \times sin(\theta) \times cos(\theta)})^2 \tag{7.3}$$

where W_y is the width of each yarn and N_y is the number of yarns forming the braid.

Analyzing a unitary braid cell such as the one schematized in Fig. 7.3, the cover factor would be CF=1-(EFGH/ABCD), with EFGH and ABCD being the areas of the corresponding polygons. When a braid is extended, the exposed area of each cell (EFGH in Fig. 7.3) reduces with decreasing braid angles until approximately zero area is left exposed (CF≈1). At this point, adjacent yarns contact each other, preventing the braid's
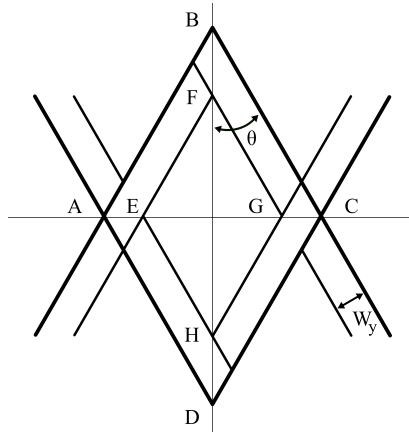
Figure 7.3: 2D projection of biaxial braid unitary cell.

diameter from further reducing and, consequently, impeding the braid's length from increasing. Through Eq. 7.3 we verify that braids with lower number of yarns (N_y) and/or lower yarn widths (W_y) have lower CF values for a given braid angle, resulting in more contractible braids.

One last consideration is that the higher the maximum exposed area within each cell, which occurs at $\theta = 45^{\circ}$, the greater the risk of the inflatable bladder bubbling through the braid and rupturing.

7.2.3 End Terminals

One particularly important design decision was having both of the heating element's electrical connectors passing through a single end terminal, as seen in Fig. 7.4. Initial prototypes were made where each terminal supported one electrical connector for the heating element. This was initially thought to be the best option to avoid accidental contact between the heating element and the inflatable bladder, as it would always keep the heating coil slightly stretched and thus centered. However, these early prototypes failed consistently after approximately one to two weeks of intermittent use. The cause of failure was always heating coil fatigue breaking due to cyclic mechanical and thermal loads (see Fig. 7.5). Also, during analysis of the failed actuators a significant amount of particulate material was found, thought to be alluminum oxide particles (Al_2O_3). The brittle passive layer of Al_2O_3, which forms on the surface of the FeCrAl heating element, breaks and chips away as the coil is repeatedly extended and contracted. In latter prototypes, where the heating element was supported by only one end terminal, a vast reduction in particulate material was observed after identical work cycles. None of these latter actuators

Figure 7.4: Actuator half assembly: lower-end terminal; static port; electric connectors and heating element.

Figure 7.5: Heating element fatigue failure.

failed due to fatigue after more than 1 month of similar intermittent testing.

7.3   Sensors

A pressure sensor (ABPDANV060PGAA5 from Honeywell) was connected to each actuator's static port through a small soft polyurethane pneumatic tube (TUS0425 from SMC). To avoid unnecessary feedback lag caused by the externally-mounted sensor, each actuator was tested with its static pressure port on the lower side, ensuring pressure was always transmitted to the sensor through liquid fluid, with negligible compressibility and thus negligible flow and pressure loss.

In some prototypes, a temperature sensor was also installed (DS18B20 from Maxim Integrated).

7.4   Manufacturing

First, all 3D-Printed components were fabricated using a regular FDM 3D-Printer (Hephestos 2 from BQ). These are the actuator's end terminals and end supports, as well as the mold for the silicone-rubber parts.

Two 7 cm segments of 1.5 mm^2 section solid copper wire were inserted through the appropriate holes in one of the 3D printed terminals. The end support was then glued to the end terminal with a cyanoacrylate adhesive (Power Flex Gel from Loctite). Excess adhesive should seep into the small crater designed around the copper wire's exit, helping to further seal the terminal.

For the silicone versions, the respective two-part material was poured into a small plastic container and thoroughly stirred. Mixing proportions were measured by mass using a precision scale.

In the same plastic container, the mixture was placed inside a vacuum chamber (model VC3028A from vacuumchambers.eu) connected to a rotary vane pump (model VP160 from Sino-Cool) and degassed for approximately 3 minutes, until no bubbles were visible coming out of the material. Degasing time may vary depending on material quantity, container geometry and vacuum chamber performance.

The silicone was then slowly poured inside the mold without its center core installed. Holding the mold at an angle and not rushing this step helps avoid trapping air bubbles inside the silicone. After filling the mold up to 2~3 cm from the brim, the center core was carefully inserted and the excess silicone was removed. The set was then degassed again for 2~5 min, to remove any air trapped during the mold pouring process, and left to cure at ambient pressure and temperature for the amount of time prescribed by the manufacturer (3 h. for EcoFlex; 24 h. for Smooth-Sil).

After curing, the silicone inflatable bladder was gently removed from the mold using compressed air.

Both the braided shell and the inflatable bladder were cut to length.

The heating element's FeCrAl coil was also cut to length, stretched, and connected to the silicone insulated wires using electric wire ferrules stripped of their plastic covers and crimped at both ends. These wires were also soldered to the main electric connectors already installed in the end terminal, forming the assembly seen in Fig. 7.4. To avoid water decomposition through electrolysis, all exposed wires and connections (except the FeCrAl coil itself) were insulated with a thin layer of epoxy. The FeCrAl coil will electrically insulate itself from the water by forming a thin passive layer of aluminum oxide (Al_2O_3).

The static pressure port was glued in place with the same cyanoacrylate adhesive used previously, and final actuator assembly was performed.

The final step was to fill in the actuator with water, through its static pressure port, with the help of a syringe.

Chapter 8

Control

A simple yet effective Actuator Driver System (ADS) was developed. It is composed of an 8bit microcontroller board (Arduino Uno Rev3) and a L298P-based DC motor controller shield (DRI0009 from DFRobot). The system receives feedback from the actuator's pressure sensor and an input set pressure signal from an external serial client/user. It runs a closed-loop Proportional-Integral (PI) control algorithm, and sends electric current to the actuator's heating element.

8.1 Feedback

To operate as a Single Input Single Output (SISO) system, pressure and temperature would be the only safe options as singular feedback signals.
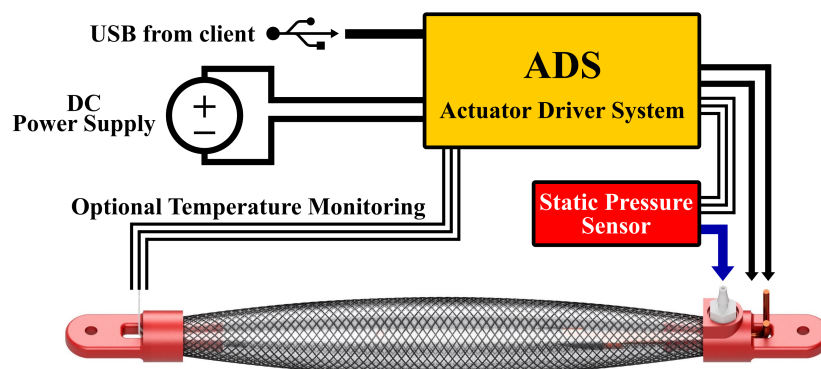

Figure 8.1: System wiring diagram.

Taking linear displacement measurements as single feedback could result in rupture if the actuator was to be mechanically constrained or overloaded, as it would be "blind" to the abnormal increase in internal pressure. Similarly, using force measurements as single input would be inadequate as the maximum allowable force (ie, the force at maximum pressure) varies along the actuator's displacement range, reaching a limit of zero force (at maximum pressure) when the actuator achieves its fully contracted state. Electrical measurements would also be impropriate as single feedback signals, since heat dissipation rates are dependent on a variety of other internal and external factors (ambient and internal temperature, air flow, actuator displacement, etc...).

Temperature feedback was considered, as it would allow for smaller and easier to integrate sensors. However, as will be shown and discussed in the Experimental Results section, pressure-based feedback allowed for far more precise and responsive control.

8.2   Algorithm

A block-diagram representation of the PI control algorithm used is presented in Fig. 8.2.

Proportional and integral coefficients (K_p and K_i respectively) were set by using a programmable power supply to perform manual control of a latex-based actuator while simultaneously recording voltage and pressure data. After a few minutes of manual control, recorded data was processed using a combination of MATLAB's System Identification Toolbox and MATLAB's PID Tuner to get an approximation of both K_p and K_i coefficients.

The controller output is an 8-bit value that defines the PWM duty cycle sent to the motor controller shield powering the actuator. A saturation limit (equal to $2^8-1=255$) prevents integral windup.

When first turned on, the ADS also runs an automatic preheat cycle, seen in Fig. 8.3, where the actuator is slowly pressurized up to a predefined internal pressure (~60% of its maximum rated pressure) at a limited power setting. This power setting was experimentally determined to be the highest possible value (to shorten the preheat cycle time), while not causing excessive subcooled pool boiling.

Subcooled pool boiling manifests itself as violent vibrations of the actuator, and should be avoided at all costs as it damages the heating element's
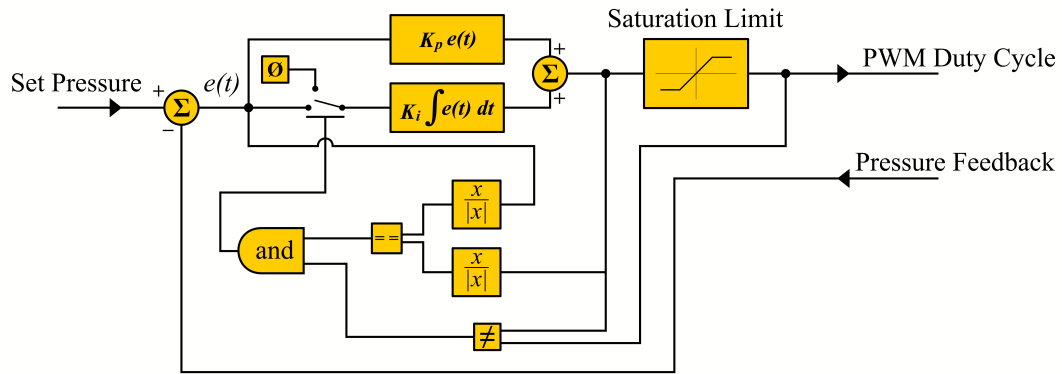
Figure 8.2: Control diagram.

protective passive layer of Al_2O_3 with the impact of high-frequency shock-waves.

Pressure oscillations, observable in the steps of Fig. 8.3, were considered acceptable and thus not worthy of expending the extra memory and computing time required for more complex control algorithms. Also, the controller's parameters were not readjusted for each specific actuator size/material, having been initially adjusted for a 150 mm latex actuator and then used successfully with the same parameters on all 100 mm, 150 mm and 200 mm latex variants, as well as 150 mm EcoFlex 00-30, EcoFlex 00-50 and Smooth-Sil 940 variants, demonstrating higher-than-expected controller robustness.

Figure 8.3: Starting and control sequence of a latex actuator.

Chapter 9

Testing and Modeling

9.1 Testing Setup

A custom-made test rig was developed to perform isometric (constant strain) and isotonic (constant stress) tests. Force measurements were made using a parallel beam load cell (TAL220B from HT Sensor Technology Co.), connected to an HX711 amplifier and an STM Nucleo 64 board. Displacement measurements were performed using a Polhemus Liberty system. Both were calibrated and tested for a precision of +- 0.02 N and +- 0.5 mm respectively.
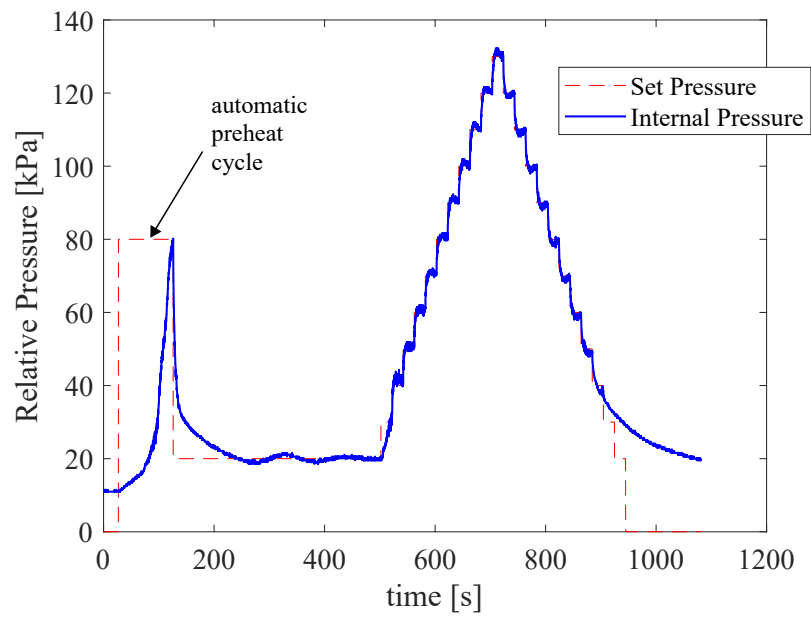
Internal temperature and pressure were measured and collected by the actuator's own sensors and control system. An external computer running a MATLAB script was used to receive, monitor and store all the synchronized data from all the sensors in both the actuator and the test rig.

9.2 Experimental Results

9.2.1 Isometric Tests

Isometric tests were first performed. Each actuator was mechanically constrained to its non-contracted length and all demonstrated an almost perfect linear correlation between force and pressure values as seen in Fig. 9.1b. As expected, the dF/dP slope decreases with an increase in stiffness. Smooth-Sil 940 has a 100% modulus of 1379 kPa, compared to 83 kPa and 69 kPa for EcoFlex 00-50 and 00-30, respectively. No mechanical properties were provided by the latex tube's manufacturer.
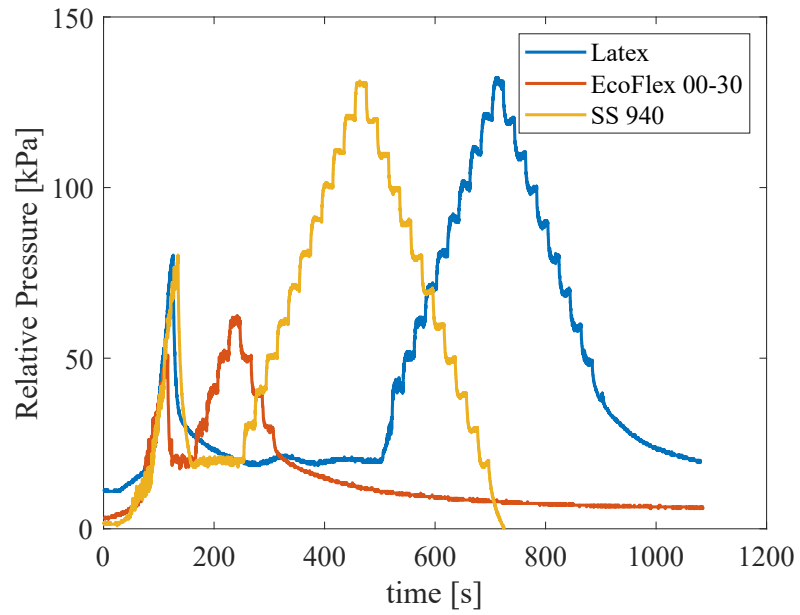
(a) Pressure-time
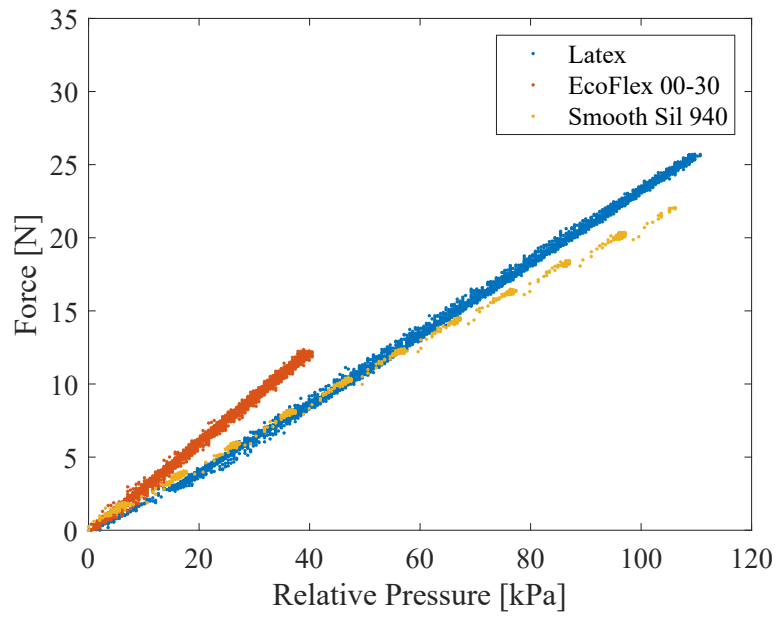
(b) Pressure-force

Figure 9.1: Isometric step test data.
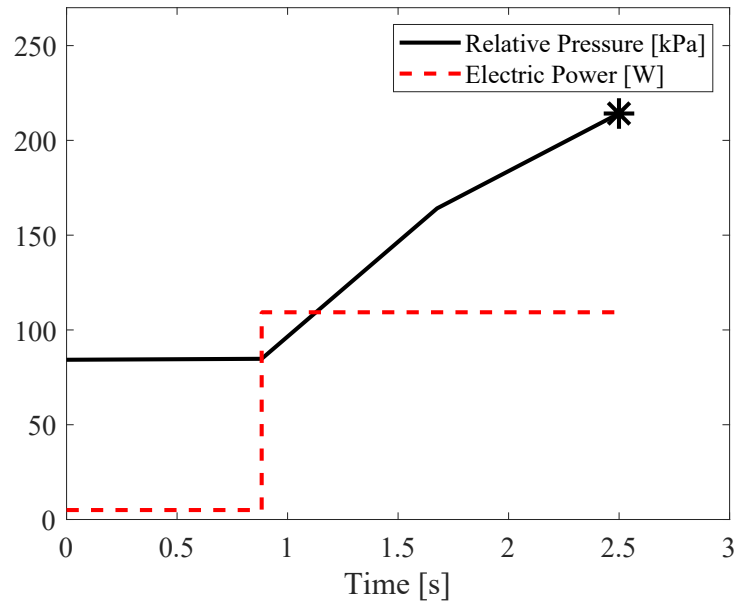
Figure 9.2: Internal pressure increase under 110 W of electrical power.

Next, we attempted to verify the assumption that the pressurization rate's limiting factor was related to the maximum heat dissipation rate and not the Critical Heat Flux. To do so, an isometric shock test was performed. A latex actuator was connected directly to our programmable DC power supply (Model 72-2540 from TENMA). A MATLAB version of the control algorithm was adapted to communicate directly with the power supply via serial connection. This allowed us to bypass the 25 W limit of our Arduino-based driver system. Then, the system was powered up and the actuator was commanded to maintain a relative pressure of 85 kPa. Shortly after stabilizing at the commanded pressure, 110 W of electrical power (3.65 A at the power supply's maximum tension of 30 V) was sent to the actuator. As seen in Fig. 9.2, a pressurization rate of 100 kPa/s was achieved, with the actuator rupturing at 214 kPa relative pressure – 165% of our proposed maximum safe operating pressure of 130 kPa. During the test, neither did the heating element burn out nor did it glow red, strongly suggesting the bulk of heat transfer between it and the fluid was still occurring through solid-liquid convection and not solid-gas convection plus radiation, at much higher temperatures, as would be expected if the CHF had been achieved.

Knowing the maximum pressurization rate to be somewhere over 100 kPa/s, we then pressurized an identical prototype to relative 210 kPa (close to the previous test's bursting pressure), and then suddenly cut
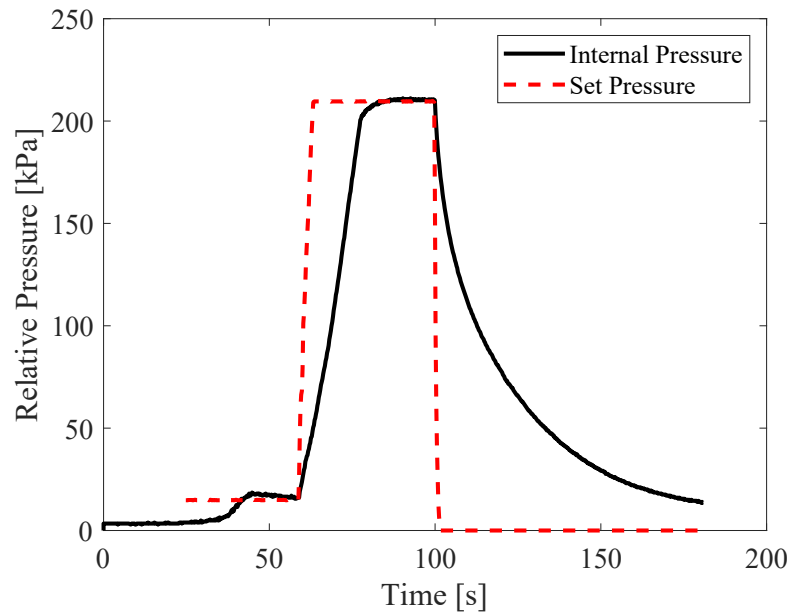
Figure 9.3: Isometric depressurization from 210kPa (relative pressure).

off electrical power. Results are plotted on Fig. 9.3. The highest observed depressurization rate was measured at -35.8 kPa/s, reducing to -7.1 kPa/s at 130 kPa and -0.5 kPa/s at our stand-by pressure of 20 kPa, proving our assumption to be correct.

One last isometric test was performed to explore the viability of performing closed-loop control using internal temperature readings. A temperature sensor was integrated on the upper-end terminal of a latex actuator. Placing the sensor on the top end of the actuator should allow it to be completely immersed in the gaseous phase – which is saturated steam – avoiding contact with the liquid phase which may be significantly subcooled especially in areas further away from the heating element. The idea was that, although with significant lag, measured temperature values should closely follow the saturation temperature of the fluid corresponding to each measured value of internal pressure. Results are plotted on Fig. 9.4.

As we may observe, measured temperature values were consistently lower than the calculated saturation temperature correspondent to the measured internal pressure values.
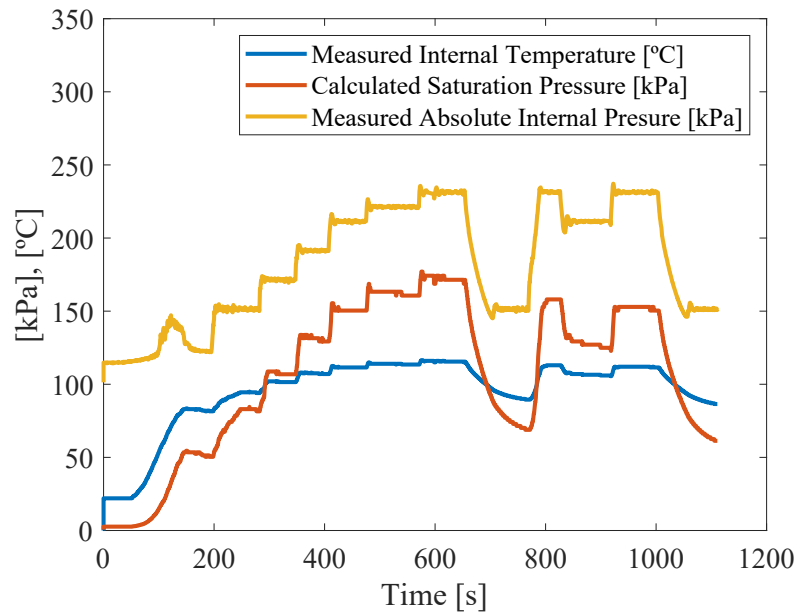
Figure 9.4: Internal absolute pressure, internal temperature and theoretical saturation temperature calculated at measured pressure.

To find the root cause of this discrepancy, first both pressure and temperature sensors were tested for accuracy.

The pressure sensor was connected in parallel with three other sensors (two identical plus a MPX4250AP from NXP Semiconductors) to an air reservoir, which was slowly pressurized from ambient pressure up to 150 kPa relative pressure. The maximum deviation between all four sensors was 1 kPa, leading us to believe pressure readings in Fig. 9.4 are valid. The latex actuator was then disassembled and its upper-end terminal – with the temperature sensor installed – was submersed in boiling water at ambient pressure. The measured value was 99 ℃, so a faulty temperature sensor was also deemed unlikely.

Although no further tests were performed to validate our theory, we argue that the tight gap between the temperature sensor's shell and the actuator's inflatable bladder allowed small droplets of condensate to adhere and fill the gap, creating a thermal bridge between the sensor and the inflatable bladder. Either way, even if temperature measurements closely matched the saturation temperature, their 2-second signal lag compared to pressure feedback would still make it inappropriate to be used as single feedback.

9.2.2 Isotonic Tests

Isotonic (ie. constant load) tests then followed, first with the actuators lifting a residual mass of 90 g (the mass of supporting hardware and sensors). Both EcoFlex-based actuators reached strains of over 20% and failed before reaching our reference pressure command of 60 kPa. The failure point in both cases was a burn hole in the inflatable bladder. The combination of low load with high deformation made this outcome expectable, as the position of the heating element had previously been determined to ensure permanent liquid immersion in a vertically mounted actuator at half the strain (10%) when operating at maximum pressure (130 kPa relative pressure).

The same test was then repeated under a much higher load of 10.8 N. No actuator failed under load. The test profile consisted of five pressurization/depressurization cycles at reduced speeds of 1 kPa/s. This demonstrated near immeasurable hysteresis (as seen in Fig. 9.5) consistent with the behavior of traditional pneumatic McKibben actuators observed by Chou and Hannaford [10]. We also noted that static friction between the inflatable bladder and the inner walls of the braided sleeve was high enough to prevent any noticeable slippage between the two. This means the small observed hysteresis should be caused mainly by yarn on yarn friction, consistent with prior observations by Tondu and Lopez [56].

9.2.3 Water Decomposition

After prolonged tests of early actuator prototypes, which were operated continuously for at least 1h, it was noticed that internal pressure at ambient temperature stabilized 8~10 kPa above the initial values measured before the test, suggesting a significant decomposition of water was occurring during operation. A simple test was performed where one actuator's end terminal was submerged in distilled water (the same used as work fluid) and connected to a 16 V (DC) power supply. Almost immediately gas bubbles could be seen forming around the exposed copper terminals (Fig. 9.6). Although electrolysis of pure water is possible, recent work suggests it would likely occur at much smaller electrode gaps [4], raising questions about the true purity of the water used in our work.

The hydrogen and oxygen mixture resultant from water electrolysis presents a long known explosion hazard [48]. In latter prototypes, exposed con-
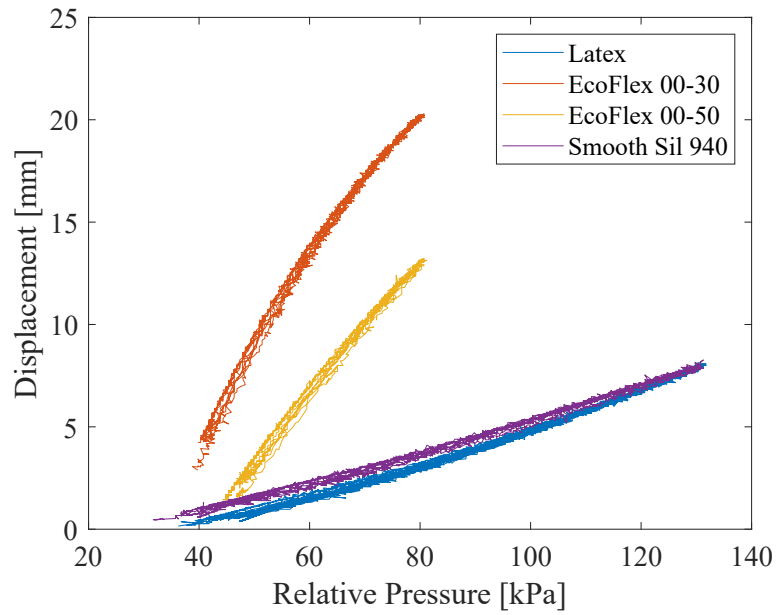
Figure 9.5: Displacement-pressure hysteresis cycles under 10.8 N constant load.

Figure 9.6: Water electrolysis occurring in the actuator's end terminal connected to a 16 V (DC) power supply.

nectors were insulated with a thin layer of epoxy resin, as described in Section 7.4. This proved effective in solving the problem.

Chapter 10

Static Model

Although our driver system demonstrated accurate and robust control, its commands take the form of set pressure values. It would be more meaningful from a user's perspective to send set force or set displacement commands, since we're dealing with a linear actuator. A model can be derived which relates all three variables: pressure; force and displacement. Any two of the former must be known to determine the third, making it necessary to install an additional sensor for control, unless the actuator is operating in either an isotonic or an isometric configuration.

Several authors have proposed models for traditional pneumatic McKibben actuators, all of which could be adapted to our case.

We derived a simple semi-empirical model inspired by the work of Chou and Hannaford [10], which takes the form of Eq. 10.1 (detailed deduction presented on Support Material 04).

$$P(F, x) = F \times \frac{4\pi n^2}{3L^2 - b^2} + P_0(x) \tag{10.1}$$

where F is the longitudinal force [N], n is the number of turns each yarn makes around the braided sleeve, L is the actuator's active length [m] and $P_0(x)$ is a 2nd-degree polynomial fitted to the actuator's response under no external load (free stroke).

It's important to note that more complex models are computationally more expensive. This must be considered when selecting or deriving more comprehensive models, which may be more precise but impractical to run on the driver system's hardware.

Seen in Fig. 10.1 is the pressure-displacement data from the previous 10.8 N isotonic test on the EcoFlex 00-30 actuator. The proposed model
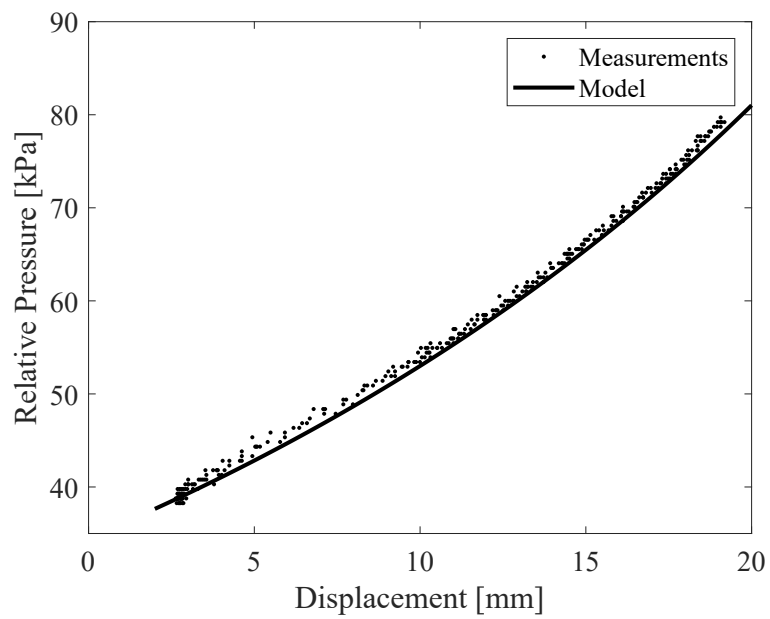
Figure 10.1: Static model and real data from 10.8 N isotonic test of an EcoFlex 00-30 actuator.

closely follows experimental results. Detailed application of the model and further discussion are presented in Support Material 04.

Chapter 11

Conclusion and Future Work

Precise pressure control of a McKibben-style phase-change actuator was demonstrated to be not only possible, but also simpler and more robust than previously thought.

This work demonstrated the limited heat dissipation rate to be the current bottleneck in phase-change soft actuator speed. It also demonstrated the achievability of extremely high pressurization rates of over 100 kPa/s. Actuators featuring soft silicone inflatable bladders proved to be difficult to control without mechanical load. Water's high specific heat resulted in long preheat cycles spawning close to 3 minutes until the actuator was ready to accept commands. Water's high enthalpy of vaporization however does not seem to be as severe a limiting factor as some authors suggest, at least in an ideal isobaric expansion setting, although further work must be done to validate this hypothesis.

The presented actuators were designed to operate in a near-vertical position – to ensure constant liquid immersion of the heating element – which is a limitation of the current design. They may operate horizontally at lower power settings (which were not tested), but future designs should feature higher heating element area, and its maximum nominal power should be determined on the basis of its surface never exceeding the inflatable bladder's maximum allowable temperature, either when in contact with the liquid phase; the gaseous phase; or in direct contact with the bladder's surface.

Finally, the presented actuator demonstrated maximum static forces well in excess of 100 times its own weight (under normal operating conditions, 27.5 N were routinely achieved with a 23 g actuator) and deformations of over 20%, in line with traditional pneumatic McKibben artificial muscles.

Bibliography

[1] E. Acome, S. K. Mitchell, T. G. Morrissey, M. B. Emmett, C. Benjamin, M. King, M. Radakovitz, and C. Keplinger. Hydraulically amplified self-healing electrostatic actuators with muscle-like performance. *Science*, 359(6371):61–65, 2018.

[2] Kaspar Althoefer. Antagonistic actuation and stiffness control in soft inflatable robots. *Nature Reviews Materials*, 3(6):76–77, 2018.

[3] António Amorim, Diana Guimares, Tiago Mendona, Pedro Neto, Paulo Costa, and António Paulo Moreira. Robust human position estimation in cooperative robotic cells. *Robotics and Computer-Integrated Manufacturing*, 67(August 2020):102035, 2021.

[4] Koichi Jeremiah Aoki, Chunyan Li, Toyohiko Nishiumi, and Jingyuan Chen. Electrolysis of pure water in a thin layer cell. *Journal of Electroanalytical Chemistry*, 695(February):24–29, 2013.

[5] Paul Badger. Capacitive Sensing Library, 2018.

[6] Nicholas W Bartlett, Michael T Tolley, Johannes T. B. Overvelde, James C. Weaver, Bobak Mosadegh, Katia Bertoldi, George M. Whitesides, and Robert J. Wood. Robot Powered By Combustion. *Science*, 349(July):161–165, 2015.

[7] Joran W. Booth, Dylan Shah, Jennifer C. Case, Edward L. White, Michelle C. Yuen, Olivier Cyr-Choiniere, and Rebecca Kramer-Bottiglio. OmniSkins: Robotic skins that turn inanimate objects into multifunctional robots. *Science Robotics*, 3(22):1–10, 2018.

[8] Mustafa Boyvat, Daniel M. Vogt, and Robert J. Wood. Ultrastrong and High-Stroke Wireless Soft Actuators through Liquid–Gas Phase Change. *Advanced Materials Technologies*, 4(2):1–6, 2019.

[9] Julian Castellanos-Ramos, Andres Trujillo-Leon, Rafael Navas-Gonzalez, Francisco Barbero-Recio, Jose Antonio Sanchez-Duran,

Oscar Oballe-Peinado, and Fernando Vidal-Verdu. Adding proximity sensing capability to tactile array based on off-the-shelf FSR and PSoC. *IEEE Transactions on Instrumentation and Measurement*, 69(7):4238–4250, 2020.

[10] Ching Ping Chou and Blake Hannaford. Measurement and modeling of McKibben pneumatic artificial muscles. *IEEE Transactions on Robotics and Automation*, 12(1):90–102, 1996.

[11] S. Davis and Darwin G. Caldwell. Braid effects on contractile range and friction modeling in pneumatic muscle actuators. *International Journal of Robotics Research*, 25(4):359–369, 2006.

[12] Artem Dementyev, Hsin Liu Cindy Kao, and Joseph A. Paradiso. SensorTape: Modular and programmable 3D-aware dense sensor network on a tape. *UIST 2015 - Proceedings of the 28th Annual ACM Symposium on User Interface Software and Technology*, pages 649–658, 2015.

[13] R. S. Diteesawat, T. Helps, M. Taghavi, and J. Rossiter. Electro-pneumatic pumps for soft robotics. *Science Robotics*, 6(51):1–12, 2021.

[14] Martin Garrad, Gabor Soter, Andrew T. Conn, Helmut Hauser, and Jonathan Rossiter. Driving soft robots with low-boiling point fluids. *RoboSoft 2019 - 2019 IEEE International Conference on Soft Robotics*, pages 74–79, 2019.

[15] Davide Giovanelli and Elisabetta Farella. Force Sensing Resistor and Evaluation of Technology for Wearable Body Pressure Sensing. *Journal of Sensors*, 2016(February), 2016.

[16] Hyo Seung Han, Junwoo Park, Tien Dat Nguyen, Uikyum Kim, Soon Cheol Jeong, Doo In Kang, and Hyouk Ryeol Choi. A flexible dual mode tactile and proximity sensor using carbon microcoils. *Electroactive Polymer Actuators and Devices (EAPAD) 2016*, 9798:979838, 2016.

[17] Jie Han, Weitao Jiang, Dong Niu, Yiding Li, Yajun Zhang, Biao Lei, Hongzhong Liu, Yongsheng Shi, Bangdao Chen, Lei Yin, Xiaokang Liu, Donglin Peng, and Bingheng Lu. Untethered Soft Actuators by LiquidâVapor Phase Transition: Remote and Programmable Actuation. *Advanced Intelligent Systems*, 1(8):1970080, 2019.

[18] Qiguang He, Zhijian Wang, Yang Wang, Zijun Wang, Chenghai Li, Raja Annapooranan, Jian Zeng, Renkun Chen, and Shengqiang Cai. Electrospun liquid crystal elastomer microfiber actuator. *Science Robotics*, 6(57):eabi9704, 2021.

[19] Kenya HIGASHIJIMA, Tomonori KATO, Kazuki SAKURAGI, Takahiro SATO, and Manabu ONO. Development of Manipulator Using a GasâLiquid Phase-Change Actuator. *JFPS International Journal of Fluid Power System*, 11(3):70–74, 2019.

[20] Dana Hughes, John Lammie, and Nikolaus Correll. A Robotic Skin for Collision Avoidance and Affective Touch Recognition. *IEEE Robotics and Automation Letters*, 3(3):1386–1393, 2018.

[21] J. A.E. Hughes, P. Maiolino, and F. Iida. An anthropomorphic soft skeleton hand exploiting conditional models for piano playing. *Science Robotics*, 3(25):1–13, 2018.

[22] Josie Hughes and Fumiya Iida. Tactile Sensing Applied to the Universal Gripper Using Conductive Thermoplastic Elastomer. *Soft Robotics*, 5(5):512–526, 2018.

[23] Masoud Kalantari, Javad Dargahi, Jozsef Kövecses, Mahmood Ghanbari Mardasi, and Shahrzad Nouri. A new approach for modeling piezoresistive force sensors based on semiconductive polymer composites. *IEEE/ASME Transactions on Mechatronics*, 17(3):572–581, 2012.

[24] Dong Jin Kang, Seongpil An, Alexander L. Yarin, and Sushant Anand. Programmable soft robotics based on nano-textured thermo-responsive actuators. *Nanoscale*, 11(4):2065–2070, 2019.

[25] Glenn K. Klute, Joseph M. Czerniecki, and Blake Hannaford. McKibben artificial muscles: Pneumatic actuators with biomechanical intelligence. *IEEE/ASME International Conference on Advanced Intelligent Mechatronics, AIM*, pages 221–226, 1999.

[26] Cecilia Laschi, Barbara Mazzolai, and Matteo Cianchetti. Soft robotics: Technologies and systems pushing the boundaries of robot abilities. *Science Robotics*, 1(1):1–11, 2016.

[27] Han Joo Lee, Noe Melchor, Hayoung Chung, and Kenneth J. Loh. Characterization of a Soft Gripper with Detachable Fingers through Rapid Evaporation. In *2020 3rd IEEE International Conference on Soft Robotics, RoboSoft 2020*, pages 83–88. Institute of Electrical and Electronics Engineers Inc., may 2020.

[28] Haojian Lu, Mei Zhang, Yuanyuan Yang, Qiang Huang, Toshio Fukuda, Zuankai Wang, and Yajing Shen. A bioinspired multilegged soft millirobot that functions in both dry and wet conditions. *Nature Communications*, 9(1), 2018.

[29] Wang Luheng, Ding Tianhuai, and Wang Peng. Influence of carbon black concentration on piezoresistivity for carbon-black-filled silicone rubber composite. *Carbon*, 47(14):3151–3157, 2009.

[30] Jeremy A. Marvel. Sensors for safe, collaborative robots in smart manufacturing. *Proceedings of IEEE Sensors*, 2017-Decem:1–3, 2017.

[31] Takahiro Matsuno, Zhongkui Wang, Kaspar Althoefer, and Shinichi Hirai. Adaptive update of reference capacitances in conductive fabric based robotic skin. *IEEE Robotics and Automation Letters*, 4(2):2212–2219, 2019.

[32] Aslan Miriyev, Kenneth Stack, and Hod Lipson. Soft material for soft actuators. *Nature Communications*, 8(1):1–8, 2017.

[33] Shane K. Mitchell, Xingrui Wang, Eric Acome, Trent Martin, Khoi Ly, Nicholas Kellaris, Vidyacharan Gopaluni Venkata, and Christoph Keplinger. An Easy-to-Implement Toolkit to Create Versatile and High-Performance HASEL Actuators for Untethered Soft Robots. *Advanced Science*, 6(14), 2019.

[34] Indrek Must, Edoardo Sinibaldi, and Barbara Mazzolai. A variable-stiffness tendril-like soft robot based on reversible osmotic actuation. *Nature Communications*, 10(1), 2019.

[35] Koya Narumi, Hiroki Sato, Kenichi Nakahara, Young Ah Seong, Kunihiko Morinaga, Yasuaki Kakehi, Ryuma Niiyama, and Yoshihiro Kawahara. Liquid Pouch Motors: Printable Planar Actuators Driven by Liquid-to-Gas Phase Change for Shape-Changing Interfaces. *IEEE Robotics and Automation Letters*, 5(3):3915–3922, 2020.

[36] Tien Dat Nguyen, Tae Sung Kim, Jiho Noh, Hoa Phung, Hyouk Ryeol Choi, and Gitae Kang. Skin-type proximity sensor by using the change of electromagnetic field. *IEEE Transactions on Industrial Electronics*, 0046(c):1–1, 2020.

[37] Zhen Zhou Nie, Bo Zuo, Meng Wang, Shuai Huang, Xu Man Chen, Zhi Yang Liu, and Hong Yang. Light-driven continuous rotating Möbius strip actuators. *Nature Communications*, 12(1), 2021.

[38] Ryuma Niiyama, Akihiko Nagakubo, and Yasuo Kuniyoshi. Mowgli: A bipedal jumping and landing robot with an artificial musculoskeletal system. *Proceedings - IEEE International Conference on Robotics and Automation*, (April):2546–2551, 2007.

[39] Alberto Oliveri, Martina Maselli, Matteo Lodi, Marco Storace, and Matteo Cianchetti. Model-based compensation of rate-dependent hysteresis in a piezoresistive strain sensor. *IEEE Transactions on Industrial Electronics*, 66(10):8205–8213, 2019.

[40] Gaoyang Pang, Geng Yang, Wenzheng Heng, Zhiqiu Ye, Xiaoyan Huang, Hua Yong Yang, and Zhibo Pang. CoboSkin: Soft Robot Skin with Variable Stiffness for Safer Human-Robot Collaboration. *IEEE Transactions on Industrial Electronics*, 68(4):3303–3314, 2021.

[41] Ron Pelrine, Roy Kornbluh, Qibing Pei, and Jose Joseph. High-speed electrically actuated elastomers with strain greater than 100%. *Science*, 287(5454):836–839, 2000.

[42] Rolf Pfeifer, Max Lungarella, and Fumiya Iida. Self-organization, embodiment, and biologically inspired robotics. *Science*, 318(5853):1088–1093, 2007.

[43] J. H. Pikul, S. Li, H. Bai, R. T. Hanlon, I. Cohen, and R. F. Shepherd. Stretchable surfaces with programmable 3D texture morphing for synthetic camouflaging skins. *Science*, 358(6360):210–214, 2017.

[44] Steven I. Rich, Robert J. Wood, and Carmel Majidi. Untethered soft robotics. *Nature Electronics*, 1(2):102–112, 2018.

[45] Daniela Rus and Michael T. Tolley. Design, fabrication and control of soft robots. *Nature*, 521(7553):467–475, 2015.

[46] José Saenz, Roland Behrens, Erik Schulenburg, Hauke Petersen, Olivier Gibaru, Pedro Neto, and Norbert Elkmann. Methods for considering safety in design of robotics applications featuring human-robot collaboration. *International Journal of Advanced Manufacturing Technology*, 107(5-6):2313–2331, 2020.

[47] Mohammad Safeea and Pedro Neto. KUKA Sunrise Toolbox: Interfacing Collaborative Robots with MATLAB. *IEEE Robotics and Automation Magazine*, 26(1):91–96, 2019.

[48] J. W. Shipley. the Alternating Current Electrolysis of Water. *Canadian Journal of Research*, 1(4):305–358, 1929.

[49] John G. Simmons. Generalized Formula for the Electric Tunnel Effect between Similar Electrodes Separated by a Thin Insulating Film. *Journal of Applied Physics*, 34(6):1793–1803, 1963.

[50] Mark A. Skylar-Scott, Jochen Mueller, Claas W. Visser, and Jennifer A. Lewis. Voxelated soft matter via multimaterial multinozzle 3D printing. *Nature*, 575(7782):330–335, 2019.

[51] J. M. Smith, H. C. Van Ness, and M. M. Abbott. *Introduction to Chemical Engineering Thermodynamics*. McGraw-Hill International Editors, fifth edition, 1996.

[52] Bjorn Sparrman, Cosima du Pasquier, Charles Thomsen, Shokofeh Darbari, Rami Rustom, Jared Laucks, Kristina Shea, and Skylar Tibbits. Printed silicone pneumatic actuators for soft robotics. *Additive Manufacturing*, 40(January):101860, 2021.

[53] Robotics Spotlight. A gripping problem - How robots are grasping - the art of gripping. *Nature*, 557, 2018.

[54] Jiefeng Sun, Brandon Tighe, Yingxiang Liu, and Jianguo Zhao. Twisted-And-Coiled Actuators with Free Strokes Enable Soft Robots with Programmable Motions. *Soft Robotics*, 8(2):213–225, 2021.

[55] Yichao Tang, Yinding Chi, Jiefeng Sun, Tzu Hao Huang, Omid H. Maghsoudi, Andrew Spence, Jianguo Zhao, Hao Su, and Jie Yin. Leveraging elastic instabilities for amplified performance: Spine-inspired high-speed and high-force soft robots. *Science Advances*, 6(19), 2020.

[56] Bertrand Tondu and Pierre Lopez. Artificial Muscle Ro bot Act u ato r s. *Control Systems,IEEE*, 20(2):15–38, 2000.

[57] Anh Vang Tran, Xianmin Zhang, and Benliang Zhu. The Development of a New Piezoresistive Pressure Sensor for Low Pressures. *IEEE Transactions on Industrial Electronics*, 65(8):6487–6496, 2018.

[58] United Nations. *Globally Harmonized System of Classification and Labelling of Chemicals (GHS)*. New York and Geneva, fourth edition, 2011.

[59] Lucie Viry, Alessandro Levi, Massimo Totaro, Alessio Mondini, Virgilio Mattoli, Barbara Mazzolai, and Lucia Beccai. Flexible three-axial force sensor for soft and highly sensitive artificial touch. *Advanced Materials*, 26(17):2659–2664, 2014.

[60] Hewen Wang, Kai Peng, Xiaokang Liu, Zhicheng Yu, and Ziran Chen. Design and Realization of a Compact High-Precision Capacitive Absolute Angular Position Sensor Based on Time Grating. *IEEE Transactions on Industrial Electronics*, 68(4):3548–3557, 2021.

[61] Luheng Wang. Usage of Connected Structure to Eliminate Blind Area of Piezoresistive Sensor Array. *IEEE Transactions on Industrial Electronics*, 65(4):3568–3575, 2018.

[62] Owies M. Wani, Hao Zeng, and Arri Priimagi. A light-driven artificial flytrap. *Nature Communications*, 8(May):1–7, 2017.

[63] Edward L. White, Michelle C. Yuen, Jennifer C. Case, and Rebecca K. Kramer. Low-Cost, Facile, and Scalable Manufacturing of Capacitive Sensors for Soft Systems. *Advanced Materials Technologies*, 2(9):1–10, 2017.

[64] Yuanzhao Wu, Yiwei Liu, Youlin Zhou, Qikui Man, Chao Hu, Waqas Asghar, Fali Li, Zhe Yu, Jie Shang, Gang Liu, Meiyong Liao, and Run Wei Li. A skin-inspired tactile sensor for smart prosthetics. *Science Robotics*, 3(22), 2018.

[65] Guang Zhong Yang, Jim Bellingham, Pierre E. Dupont, Peer Fischer, Luciano Floridi, Robert Full, Neil Jacobstein, Vijay Kumar, Marcia McNutt, Robert Merrifield, Bradley J. Nelson, Brian Scassellati, Mariarosaria Taddeo, Russell Taylor, Manuela Veloso, Zhong Lin Wang, and Robert Wood. The grand challenges of science robotics. *Science Robotics*, 3(14), 2018.

Support Material 01

Calculation Procedure of Work/Heat Quotient During Isobaric Liquid-Gas Phase Transition.

Enthalpy of vaporization (ΔH_{vap}) across a range of saturation temperatures

Estimation of a fluid's enthalpy of vaporization at different saturation temperatures from a single known value pair can be made with Watson's widely accepted method [1], in the form of Eq. 1

$$\frac{\Delta H_1}{\Delta H_2} = (\frac{1 - T_{r1}}{1 - T_{r2}})^{0.38} \tag{1}$$

where ΔH_n [J/kg] is the enthalpy of vaporization at saturated reduced temperature T_{rn}. Reduced temperatures are a dimensionless thermodynamic coordinate, defined by Eq. 2

$$T_r = \frac{T}{T_c} \tag{2}$$

where T [K] is the fluid's actual absolute temperature, and T_c [K] is the fluid's critical temperature.

Reference values for all analyzed work fluids are summarized in Table 1.

Table 1: Work fluid physical properties

	T_{sat} @1atm [K]	T_c [K]	ΔH_{vap} @1atm [J/kg]	Molar Weight [kg/mol]
Water	373.15	647.14	2 257 000	18.015×10^{-3}
FC-72	329.15	449.15	88 000	338×10^{-3}
PF-5052	323.15	454	105 000	299×10^{-3}
PF-5060	329.15	451	88 000	338×10^{-3}
PF-5070	353.15	478	80 000	388×10^{-3}
Novec 7000	307.15	438.15	34 000	200×10^{-3}
Novec 7100	334.15	468.15	61 000	250×10^{-3}
Novec 7200	349.15	483.15	76 000	264×10^{-3}
Ethanol	351.39	516.25	855 220	46.07×10^{-3}
Acetone	329.23	508.1	512 913	29.79×10^{-3}

With data from Tab. 1, Eq. 1 may be applied over a relevant range of saturation temperatures, as plotted in Fig. 1.
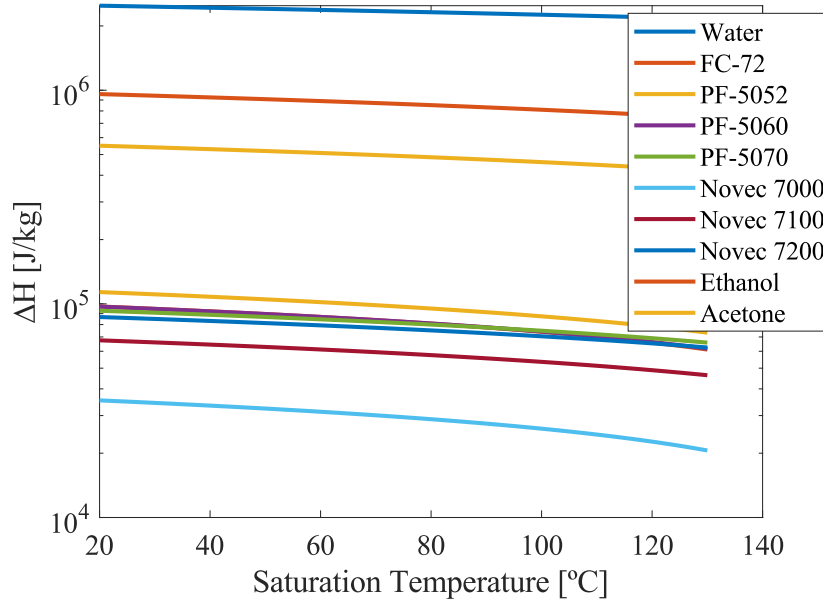
Figure 1: Enthalpy of vaporization

Pressure-temperature saturation curves

Pressure values corresponding to a given saturation temperature may be calculated from the fluid's pressure-temperature saturation curve. Equations defining this curve for all analyzed work fluids are summarized in Tab. 2, Tab. 3, and plotted in Fig. 2.

Table 2: Vapor pressure of work fluids

	Saturation Curve Eq.	Units.	Source
Water	$P_{sat} = 0.61121exp((18.678 - \frac{T}{234.5})(\frac{T}{257.14+T}))$	[kPa], [ºC]	[3]
FC-72	$P = 10^{(9.729-(1562/T))}$	[Pa], [K]	3M
PF-5052	$P = 10^{(10.062-(1643/T))}$	[Pa], [K]	3M
PF-5060	$P = 10^{(9.729-(1562/T))}$	[Pa], [K]	3M
PF-5070	$P = 10^{(10.142-(1824/T))}$	[Pa], [K]	3M
Novec 7000	$P = exp(-3548.6/T + 22.978)$	[Pa], [K]	3M
Novec 7100	$P = exp(22.415 - 3641.9 * (1/T))$	[Pa], [K]	3M
Novec 7200	$P = exp(22.289 - 3752.1 * (1/T))$	[Pa], [K]	3M

Table 3: Vapor pressure of Acetone and Ethanol [2]

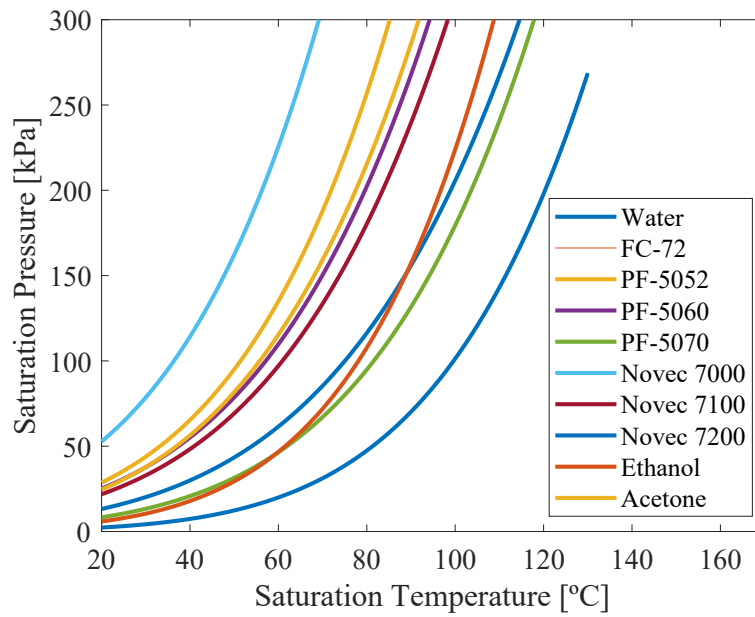| $\log_{10} P[mmHg]= A+B/T[K] +C \log_{10}T[K] + DT[K] +ET[K]^2$				
	A	B	C	D	E
Acetone	28.5884	−2.4690E+03	−7.3510E+00	2.8025E−10	2.7361E−06
Ethanol	23.8442	−2.8642E+03	−5.0474E+00	3.7448E−11	2.7361E−07

Figure 2: Saturation curves

Volumetric expansion – ΔV

Work done by the expanding fluid under isobaric conditions may be determined by Eq.3.

$$W = -P\Delta V \tag{3}$$

where ΔV is the total change in volume, and P is the pressure at which expansion took place. We consider energy to be negative when leaving the fluid, that being the reason for the minus sign in Eq.3.

The enthalpy of vaporization accompanying a phase change is related to other system properties by Eq. 4.

$$\Delta H_{vap} = T\Delta V \frac{dP_{sat}}{dT} \tag{4}$$

Eq. 4 may be rearranged to calculate the total volumetric change, Eq. 5.

$$\Delta V = \frac{\Delta H_{vap}}{T}(\frac{dP_{sat}}{dT})^{-1} \tag{5}$$

The pressure slope dP_{sat}/dT can be calculated from the saturation curve equations in Tab. 2 and ΔHvap was previously determined through Eq. 1, so we may proceed to calculate the effective volumetric change, ΔV, at each point in the fluid's saturation curve.

Work/Heat quotient

By definition, the enthalpy of a system is explicitly defined by Eq. 6.

$$H = U + PV \tag{6}$$

where U is the system's internal energy.

Since U, P and V are state functions, enthalpy (H) must also be a state function and thus any finite change in its value can be determined by Eq. 7,

$$\Delta H = \Delta U + \Delta(PV) \tag{7}$$

which, assuming isobaric expansion becomes:

$$\Delta H = \Delta U + P\Delta(V) \tag{8}$$
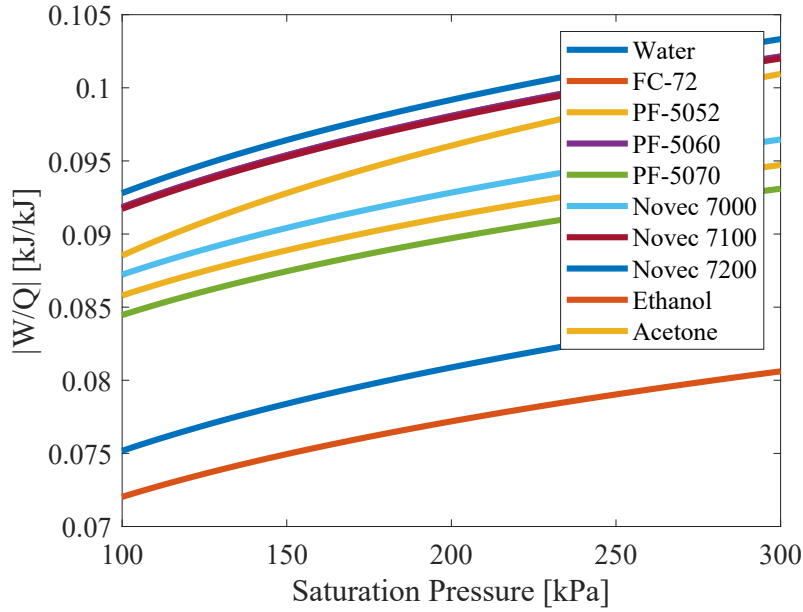
and, remembering Eq. 3 leads us to:

Figure 2: Work/Heat fraction

$$\Delta H = \Delta U - W = Q + W - W = Q \qquad (9)$$

Finally, the work/heat fraction can finally be calculated through Eq. 10.

$$\left| \frac{W}{Q} \right| = \left| \frac{-P \Delta V}{\Delta H_{vap}} \right| \qquad (10)$$

References

[1] K. M. Watson. Thermodynamics of the Liquid State: Generalized Prediction of Properties. Industrial and Engineering Chemistry, 1943

[2] A. Kayode Coker. Ludwig's Applied Process Design for Chemical and Petrochemical Plants. 4th Edition, 2007. ISBN: 9780750677660

[3] Buck, A. L., New equations for computing vapor pressure and enhancement factor, J. Appl. Meteorol., 20, 1527-1532, 1981

Support Material 02

Calculation of Inflatable Bladder Minimum Tube Length

Motivation

Convection heat transfer coefficients are generally far lower between solids and gases than they are between solids and liquids. If the actuator's heating element is ever exposed to the work fluid's gaseous phase, a drastic increase in surface temperature will occur, to compensate for the much higher thermal resistance. This increase in temperature may damage both the heating element and the surrounding inflatable bladder.

Problem

What is the minimum inflatable bladder length which ensures permanent immersion of the actuator's heating element in the liquid phase of the work fluid (water), given that all other dimensions are fixed and known?

Data

Description	Notation	Value
Braid's yarn length	b	0.1732 [m]
Yarn turns around the braid's longitudinal axis	n	2.5
Wet element volume	V_{wet}	1.5×10^{-6} [m^3]
Inflatable bladder thickness	t_k	0.002 [m]

Hypothesis

- No solved gases in the work fluid

- No generation of gases through electrolysis

- Inflatable bladder geometry approximated to remain cylindrical throughout operation

- Inflatable bladder's thickness remains constant throughout operation

- Maximum nominal pressure of 230 kPa (absolute)

- Maximum actuator deformation of 10% at maximum nominal pressure

Calculation

The mass of liquid and gas inside the actuator (M_l and M_g respectively) will always sum up to the total initial work fluid mass, which is considered time-invariant. That is:

$$M_l + M_g = M_{fluid} \tag{1}$$

Similarly, the volume of liquid and gas inside the actuator (V_l and V_g respectively) will always sum up to the total volume available inside the actuator (V_{int}), which varies with actuator deformation.

$$V_l + V_g = V_{int} \tag{2}$$

Through Eq. 1 and Eq. 2, the mass of fluid in liquid form can be related to the total mass and volume, Eq. 3.

$$M_l = \frac{V_{int} \times \rho_l \times \rho_g - M_{tot} \times \rho_l}{\rho_g - \rho_l} \tag{3}$$

where ρ_l and ρ_g represent the current density of the fluid's liquid and gaseous phases, respectively.

Both the length (L_{sleeve}) and diameter (D_{sleeve}) of the braided sleeve are functions of the varying braid angle θ:

$$D_{sleeve} = \frac{b \times sin(\theta)}{n \times \pi} \tag{4}$$

$$L_{sleeve} = b \times cos(\theta) \tag{5}$$

The braided sleeve and the inflatable bladder are equal in length, that is $L_{sleeve} = L$.

The internal volume available within the inflatable bladder (V_{int}) can then be calculated by Eq. 6:

$$V_{int} = \frac{1}{4} \times \pi \times (D_{sleeve} - 2t_k)^2 \times L - V_{wet} = \frac{\pi L}{4} * \left(\frac{b\sqrt{1 - \frac{L^2}{b^2}} - 2n\pi t_k}{n\pi} \right)^2 - V_{wet}$$

(6)

where t_k is the inflatable bladder's wall thickness, assumed constant.

A first estimate for a compatible depressurized resting length will be L_0=0.150 m, which yields a minimum length under pressure of L_{min}=(1–0.1)×0.150=0.135 m under 10% deformation. This value may need to be reiterated later.

By Eq. 6, the depressurized internal volume is V_{int}=4.31445×10^{-6} m^3 and the pressurized volume is V_{int}=8.715×10^{-6} m^3.

The total mass of fluid M_{fluid} may be calculated by multiplying the resting internal volume with the saturated liquid's density at standard ambient pressure, Eq. 7.

$$M_{fluid} = V_{int}(L_0) \times \rho_l = 4.133 \times 10^{-3} kg$$

(7)

And recovering Eq. 3, the mass of the liquid phase can now be calculated, using the properties of saturated water at the maximum rated pressure of 230 kPa:

$$M_l = \frac{V_{int} \times \rho_l \times \rho_g - M_{tot} \times \rho_l}{\rho_g - \rho_l} = 4.127 \times 10^{-3} \ kg$$

(8)

The correspondent volume of liquid is:

$$V_l = \frac{M_l}{\rho_l} = 4.394 \times 10^{-6} m^3 \tag{9}$$

Finally, the height of the liquid's free surface (h_l) can now be determined:

$$h_l = \frac{V_l \times L}{V_{int}} = \frac{4.394E - 6 \times 0.135}{8.715E - 6} = 0.068m \tag{10}$$

The top part of heating element reaches 65 mm from the end terminal to which it is connected. So, h_l=68 mm ensures the element is still immersed in the liquid phase. We then conclude that the length of the inflatable bladder must be made equal or greater to L_0=150 mm.

Support Material 03
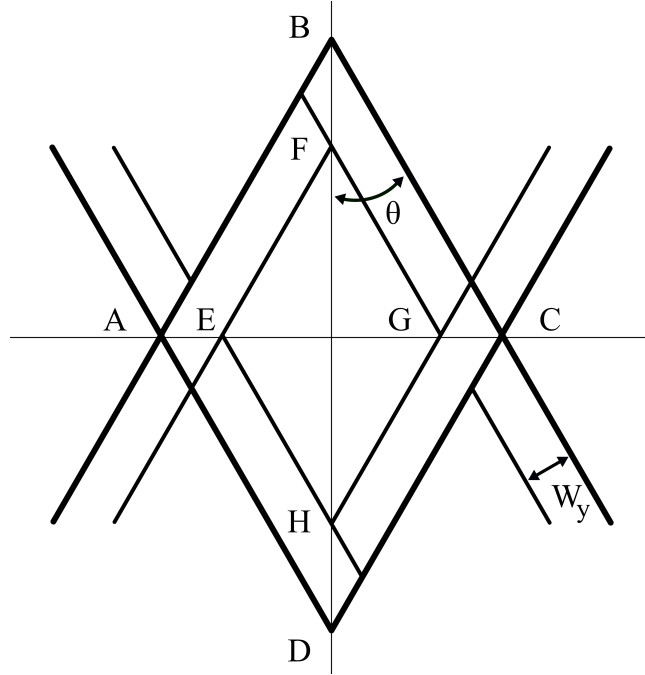
Cover Factor of a Biaxial Braided Sleeve

Figure 1: Biaxial braid unitary cell

Figure 1 represents a unitary cell on a biaxial braided sleeve.

The segments $\bar{AC}$ and $\bar{BD}$ can be determined by Eq. 1 and Eq. 2, respectively:

$$\bar{AC} = \frac{2\pi D}{N_y} \tag{1}$$

$$\bar{BD} = \frac{2\pi D}{N_y \times tan(\theta)} \tag{2}$$

where D is the braid's diameter, N_y is the number of yarns and θ is the braid angle.

The area of the polygon ABCD is then defined by Eq. 3.

$$A_{ABCD} = \frac{1}{2} \times \bar{AC} \times \bar{CD} = \frac{2\pi^2 D^2}{N_y^2 \times tan\,(\theta)} \tag{3}$$

Similarly, segments $\bar{EG}$ and $\bar{FH}$ can be determined by Eq. 4 and Eq. 5, respectively:

$$\bar{EG} = \bar{AC} - 2 \times \bar{AE} = \frac{2\pi D}{N_y} - 2 \times \frac{W_y}{cos\,(\theta)} \tag{4}$$

$$\bar{FH} = \bar{BD} - 2 \times \bar{BF} = \frac{2\pi D}{N_y tan\,(\theta)} - 2\frac{W_y}{sen\,(\theta)} \tag{5}$$

where W_y Is the width of each yarn.

The area of the polygon EFGH is then defined by Eq. 6.

$$A_{EFGH} = \frac{1}{2} \times \bar{EG} \times \bar{FH} = \frac{2}{tan\,(\theta)} \times \left(\frac{\pi D}{N_y} - \frac{W_y}{cos\,(\theta)}\right)^2 \tag{6}$$

The cover factor (CF) may then be determined as a function of D and θ, Eq. 7.

$$CF = 1 - \left(\frac{A_{EFGH}}{A_{ABCD}}\right) = 1 - (1 - \frac{W_y N_y}{\pi D cos(\theta)})^2 \tag{7}$$

The variable diameter of a given braid is a function of its braid angle θ, Eq. 8.

$$D = \frac{b \times sin\,(\theta)}{n\pi} \tag{8}$$

Where b is the length of each yarn and n is the number of turns each yarn makes around the braid's longitudinal axis.

From Eq. 7 and Eq. 8 we can derive Eq. 9, where the Cover Factor is a function of constant braid parameters (n, N_y, W_y) and the variable braid angle θ.

$$CF = 1 - \left(1 - \frac{nW_yN_y}{b * sin\left(\theta\right)cos\left(\theta\right)}\right)^2 \tag{9}$$

Support Material 04

Actuator Static Model

Ideal McKibben Pneumatic Artificial Muscle (PAM)

Consider an ideal McKibben-style pneumatic artificial muscle, characterized by:

- Zero static and dynamic friction

- Inflatable bladder made up of an infinitely soft material (with zero Young's modulus)

- Inflatable bladder made up of an infinitely thin material (with zero thickness)

- Braided sleeve made up of infinitely rigid strands

The output force of such actuator, as described by Chou and Hannaford [1], can be calculated through Eq. 1,

$$F = \frac{Pb^2}{4\pi n^2}(3 \times cos^2(\theta) - 1) \tag{1}$$

where P [Pa] is the relative internal pressure, b [m] is the fixed length of the braid's yarns, n is the number of turns each yarn makes around the braid's longitudinal axis, and θ is the variable braid angle.

Braid angle is a function of the braid's current length, as described by Eq. 2.
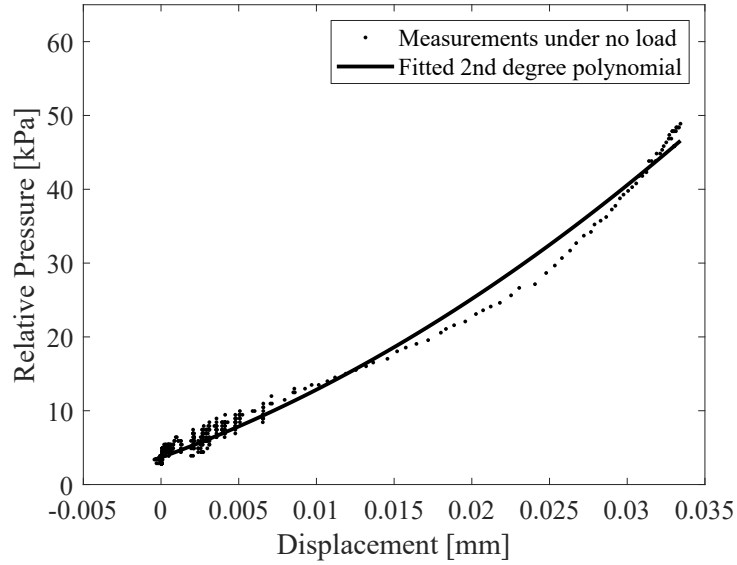
$$L = b \times cos(\theta) \tag{2}$$

Figure 1: Force-displacement data from free stroke test of a EcoFlex 00-30 actuator

From Eq. 1 and Eq. 2 one could derive Eq. 3.

$$P_{ideal} = F \times \frac{4\pi n^2}{3L^2 - b^2} \tag{3}$$

Isotonic data from real Phase Change Artificial Muscles (PCAM)

The pressure-displacement relation of our PCAM's under zero load (free stroke) isotonic tests can be closely approximated by a 2nd-degree polynomial.

Fig. 1 shows data recorded during free stroke (ie. no load) test of an EcoFlex 00-30 actuator, as well as a conveniently fitted polynomial, Eq. 4

$$P(\Delta L) = A(\Delta L)^2 + B\Delta L + C \tag{4}$$

Factor	Value
A	1.563e+07
B	-7.608e+05
C	3677

where ΔL [m] is the linear displacement of the actuator.

Semi-empirical static model

The pressure necessary to deform the real actuator is accounted for by the aforementioned empirical model, Eq. 4. The overpressure necessary to output a given force is accounted for by the ideal static model, Eq. 1. Adding the two models together results in Eq. 5

$$P(F, x) = F \times \frac{4\pi n^2}{3L^2 - b^2} + A(\Delta L)^2 + B\Delta L + C \tag{5}$$

Note that Coulomb friction was not considered in Eq. 5. An extra term accounting for this may be deemed necessary in some high load and/or high precision applications.
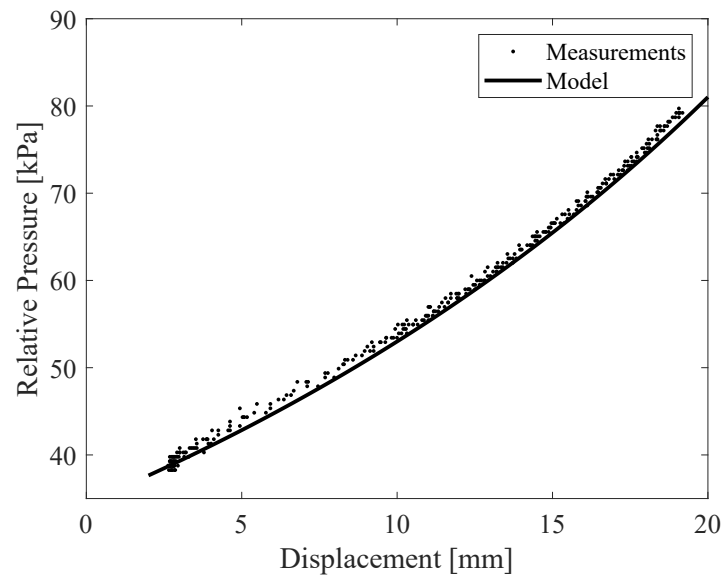
Figure 2: Model and data from 10.8N isotonic test of an EcoFlex 00-30 actuator

Model validation

To validate the aforementioned model, we now use a different data set, recorded during isotonic test of the same actuator under 10.8 N of load. Fig. 2.

References

[1] Ching Ping Chou and Blake Hannaford. Measurement and modeling of McKibben pneumatic artificial muscles. IEEE Transactions on Robotics and Automation, 12(1):90–102, 1996.